Correction date 0323; Revision 2

Cation ordering, twinning and pseudo-symmetry in silicate garnet: the study of a birefringent garnet with orthorhombic structure

Word Count: 10212

Huifang Xu[1*], Shiyun Jin[1,2], Seungyeol Lee[1,3,4], and Philip E. Brown[1]

[1]Department of Geoscience, University of Wisconsin-Madison, Madison, Wisconsin, 53706, USA

[2]Gemological Institute of America, 5355 Armada Drive, Carlsbad, CA 92008, USA

[3]USRA Lunar and Planetary Institute, 3600 Bay Area Boulevard, Houston, TX 77058, USA

[4]ARES, NASA Johnson Space Center, 2101 NASA Parkway, Houston, TX 77058, USA

*E-mail: hfxu@geology.wisc.edu

ABSTRACT

The crystal structure of a birefringent garnet (~$Adr_{53}Grs_{47}$) that occurs as a late-stage rim on andradite from Stanley Butte, Graham County, Arizona is analyzed and refined using single-crystal XRD. The structure has an orthorhombic $I\frac{2}{a}1\frac{2}{d}$ (unconventional setting for *Fddd*) space group symmetry, with unit cell parameters of $a = b = 11.966(3)$ Å, $c = 11.964(3)$ Å, $\alpha = \beta = 90°$, $\gamma = 90.29(2)°$, $V = 1713.0(7)$ Å^3, $Z = 8$. The orthorhombic garnet displays very high birefringence ($\delta \sim 0.021$) produced by the strong Fe-Al ordering in the octahedral sites, with Fe occupancies of 0.804 and 0.221 in Y_1 and Y_2 sites, respectively. Diffraction peaks (such as 101 and 103) violating the $Ia\bar{3}d$ symmetry of cubic garnet are obvious even in powder XRD pattern. The homogenization temperatures of the fluid inclusions suggest that the low crystallization temperature is responsible for the ordered orthorhombic structure. The strong ordering state of the structure and the sharp boundaries in the chemical zoning in the crystal (between ~$Adr_{53}Grs_{47}$ and ~Adr_{100}) indicate the orthorhombic intermediate grandite garnet is a thermodynamically stable phase at low temperature, separated by wide miscibility gaps from the pure end members (grossular and andradite) with cubic structures. Most of the previously reported triclinic garnet structures are likely artifacts produced by pseudo-merohedral twinning of less ordered orthorhombic structure, as indicated by the characteristic pairing pattern of different Y-sites with the same occupancies.

Keywords: orthorhombic garnet, Fe-Al ordering, non-cubic garnet, birefringent garnet, pseudo-merohedral twinning, fluid inclusion

This is the peer-reviewed, final accepted version for American Mineralogist, published by the Mineralogical Society of America.
The published version is subject to change. Cite as Authors (Year) Title. American Mineralogist, in press.
DOI: https://doi.org/10.2138/am-2022-8455. http://www.minsocam.org/

INTRODUCTION

Silicate garnets are common rock-forming orthosilicate minerals that occur in earth's crust and mantle, which have a general formula of $X_3Y_2[SiO_4]_3$, with X representing divalent cations in triangular dodecahedron (distorted cube) (i.e., Ca^{2+}, Fe^{2+}, and Mg^{2+}), and Y representing trivalent cations in regular octahedral site (i.e., Cr^{3+}, Al^{3+}, and Fe^{3+}) (Geiger 2008, 2016; Grew et al. 2013). The tetrahedrally coordinated Si site is known as Z site, which can be occupied by elements such as Al, Fe or V in non-silicate garnets (Grew et al. 2013). A significant amount of structural OH^- (water) may be incorporated in these nominally anhydrous minerals, mostly through the hydrogarnet substitution (Lager et al. 1989; Grew et al. 2013; Geiger and Rossman 2018, 2020). Although silicate garnets generally have cubic ($Ia\bar{3}d$) symmetry, birefringence is often observed in the grossular (Grs: $Ca_3Al_2Si_3O_{12}$) - andradite (Adr: $Ca_3Fe^{3+}{}_2Si_3O_{12}$) solid solution (grandite garnet). [The IMA-CNMNC approved mineral symbols (abbreviations) are used to describe the garnet compositions in this paper (Warr 2021).] Similar effects have been recently reported in the less studied uvarovite (Uv: $Ca_3Cr_2Si_3O_{12}$) – grossular solid solution (Andrut and Wildner 2001, 2002; Wildner and Andrut 2001; Andrut et al. 2002). Fine scale oscillatory zoning, supposedly related to the anisotropy, is also commonly observed in grandite garnets (Lessing and Standish 1973; Murad 1976; Jamtveit 1991; Jamtveit et al. 1993, 1995; Pollok et al. 2001; Antao 2013; Antao et al. 2015). Some of the sub-micron periodic zoning near the surface can create spectacular iridescent colors similar to those observed in labradorite, making them gemstones (Ingerson and Barksdale 1943; Akizuki et al. 1984; Hainschwang and Notari 2006; Nakamura et al. 2017).

Various reasons have been proposed to explain the optical anomaly of the calcium silicate garnets, including plastic deformation (Allen and Buseck 1988), magneto-optical effects from rare-earth elements substituting for Ca (Blanc and Maisonneuve 1973), non-cubic orientation of the OH^- groups (Rossman and Aines 1986), or residual strain from chemical zoning or twin boundaries (Chase and Lefever 1960; Lessing and Standish 1973; Foord and Mills 1978; Antao 2013a,b, 2021a,b; Antao and Klincker 2013; Antao et al. 2015). Among all the hypothesized reasons, symmetry reduction due to cation ordering remains the most widely proposed (Takéuchi and Haga 1976; Takéuchi et al. 1982; Gali 1983, 1984; Akizuki 1984, 1989, 1989; Allen and Buseck 1988; Hatch and Griffen 1989; Kingma and Downs 1989; Griffen et al. 1992; Shtukenberg et al. 2001, 2002, 2005; Frank-Kamenetskaya et al. 2007; Kobayashi et al. 2013;

Badar et al. 2016; Nakamura et al. 2016). However, the real symmetry of the birefringent calcium silicate garnets remains ambiguous with many different structures refined. The graph of all centrosymmetric subgroups of the $Ia\bar{3}d$ space group that preserves the *I*-centered translational symmetry, along with their relations to each other is shown in Figure 1. Most birefringent garnet structures were refined with triclinic $I\bar{1}$ symmetry (Takéuchi et al. 1982; Allen and Buseck 1988; Kingma and Downs 1989; Wildner and Andrut 2001; Kobayashi et al. 2013; Nakamura et al. 2016). Tetragonal garnet based on X-sites ordering in the almandine-grossular solid solution system has also been reported (Griffen et al. 1992; Cesare et al. 2019). Recently, a trigonal hydrous garnet species with ordered Fe-Al distribution in Y-sites and $Si/(OH)_4$ ordering in tetrahedral (Z) sites was discovered (Krivovichev et al. 2021). Orthorhombic garnet was first reported in a grandite garnet ($Adr_{33}Grs_{67}$) by Takéuchi and Haga (1976), however, many later studies of metrically orthorhombic garnet structures concluded they are pseudo-orthorhombic with triclinic ($I\bar{1}$) symmetry (Takéuchi et al. 1982; Shtukenberg et al. 2005; Frank-Kamenetskaya et al. 2007).

The problem is further complicated as some of the symmetry violating reflections are suspected to be produced by multiple diffraction (Rossmanith and Armbruster 1995). Twinning in anisotropic garnet has been discussed (Takéuchi et al. 1982; Hatch and Griffen 1989), yet never taken into account during structure refinements. Most of the published structure models did not include any raw diffraction data, making it difficult to judge the validity of the models. Structural analyses from powder diffraction may bypass the potential complexity introduced by twinning, but significant peak overlaps from minute lattice distortion and anisotropic strains are very difficult to resolve, which often lead to ambiguous symmetry determination (Antao 2013a; Tančić et al. 2020). The poorly understood structural model makes it hard to determine whether the cation ordering is kinetically induced during crystal growth (Shtukenberg et al. 2001, 2005; Frank-Kamenetskaya et al. 2007), or thermodynamically driven during low-temperature phase transition (Engi and Wersin, 1987; Hatch and Griffen 1989; Jamtveit 1991; Becker and Pollok, 2002), with the existing data being used to support arguments in both directions.

In this paper, we report the structure of an orthorhombic grandite garnet single crystal ($I\frac{2}{a}1\frac{2}{d}$ space group, an unconventional setting for *Fddd*) showing very high birefringence ($\delta \sim$ 0.021). The grandite crystal has much stronger Fe/Al ordering in the octahedral sites than any of

the previously published structures, with significant lattice distortion from cubic symmetry. The fluid inclusions in the samples indicate low crystallization temperatures, providing strong evidence for a thermodynamically stable phase for grandite with composition close to $Adr_{50}Grs_{50}$. The effect of twinning on the intensity distribution in the diffraction data is also discussed in detail, providing a potential explanation for previously reported structures with different space group symmetry.

SAMPLES AND EXPERIMENTAL METHODS

The specimen (UW Mineral Collection 7579) was collected from Stanley Butte, San Carlos Indian Reservation, Graham County, Arizona. The site and similar minerals were described before (Ross 1925; Anthony et al. 1995). It occurs as a gangue mineral in a skarn deposit. The euhedral crystals occur on the wall of a hydrothermal vein (Figures S1, S2, S3). The orthorhombic garnet rim that grew around early-stage andradite, formed at a very late stage (Figure 2). Associated minerals include epidote and quartz. The olive-green euhedral dodecahedral crystals range from 2 mm to 10 mm in diameter (Figure S1, 2). The orthorhombic garnet with high interference colors occurs as an outer rim (~2 mm to 4 mm thick) that coats the core andradite (Figure 2). It is colourless in thin section. Refractive indices are calculated based on average refractive index (~1.810) for the garnet composition (Deer et al. 1982, p. 486). The measured birefringence is ~ 0.021, and its 2V(+) angle is 75(5)º (see Figure S5 for its interference figure).

The chemical composition of the garnet sample was analyzed with a CAMECA SXFive field emission electron probe at 15 kV and 10 nA beam current with a 5 μm beam size, using microcline, jadeite, augite, forsterite, tephroite, fluorite, and quartz as standards. H_2O is calculated by analysing the O by EPMA and assigning the excess O to H_2O. The strongly birefringent rim shows an average composition of $(Ca_{2.91}Fe^{2+}_{0.06}Mn^{2+}_{0.02})$ $(Fe^{3+}_{1.06}Al_{0.94})$ $(Si_{2.93}\square_{0.07})$ $(O_{11.71}F_{0.14}OH_{0.15})$, or ~$Adr_{53}Grs_{47}$. The isotropic core and zones, on the other hand, show compositions close to the andradite end member. The results of the chemical analyses are listed in Table 1.

Double polished sections were used for the fluid inclusion analyses. Measurement of homogenization and freezing temperature were conducted at the University of Wisconsin-Madison using a Linkam LMS600 heating-freezing stage mounted on an Olympus BX50 microscope with a 100x objective lens. The fluid-inclusion populations in our garnet sample are predominantly monophase liquid inclusions with small numbers of two-phase inclusions, as shown in Figure 3. Our measured homogenization temperatures (T_h) of primary liquid-rich inclusions range from 157 °C to 170 °C (Figure 3). Freezing point depressions (T_m) are about -11 °C, corresponding to salinities of ~14 equiv. wt.% NaCl (Vanko et al. 1988; Bodnar 1994; Hurai et al. 2015). Previous research on skarn systems similar to the source of these garnets estimates formation pressures ranging from ~300 to ~1000 bars (Theodore et al. 1986; Boni et al. 1990; Myers 1994). Trapping temperatures for the orthorhombic garnet inclusions are estimated to be ~ 180 °C to ~220 °C by using the range of trapping pressures with the isochores appropriate for the measured T_h and salinity (Bodnar 1994).

The areas with the highest uniform interference color (see 2 circled areas inside circles in Figure 2c) were selected for single-crystal XRD work and were cut from petrographic thin sections. Twined crystals were eliminated through careful screening using single-crystal XRD method. X-ray diffraction data were collected on a Bruker Quazar APEXII single-crystal diffractometer with a MoKα IμS source and APEX2 detector. The instrument was operated at a voltage of 50 kV and current of 0.6 mA. Unit-cell parameters were calculated and refined using *APEX3* software. The refinement of the structures was performed with *JANA2006* software (Petříček et al. 2014) on F^2. The 3D crystal structure was visualized by *VESTA* (Momma and Izumi 2011). The experimental and crystallographic information are listed in Table 2. Powder XRD data were collected with a 2-D image-plate detector and a 0.1 mm collimator using a Rigaku Rapid II instrument (Mo-*K*α radiation) in the Department of Geoscience, University of Wisconsin-Madison. Two-dimensional diffraction patterns were converted to conventional 2θ vs. intensity plots using the Rigaku 2DP software. Transmission electron microscope (TEM) samples were prepared by depositing a suspension of crushed grains (picked from the thin section next to the crystal used for single-crystal XRD) on a lacy carbon-coated Cu grid. The bright-field and high-resolution TEM images with the selected-area electron diffraction (SAED) patterns were obtained using a Philips CM200-UT transmission electron microscope operated at 200 kV in the

Materials Science Center, University of Wisconsin-Madison. The chemical composition was obtained using Energy-dispersive X-ray spectra (EDS) with a Li-drifted Si detector.

RESULTS

Single-crystal XRD

Based on the body-centered lattice with no symmetry constraints, the unit-cell parameters are refined to be a = 11.967(3) Å, b = 11.965(3) Å, c = 11.964(3) Å, α = 90.00(1)°, β = 90.01(1)°, γ = 90.29(2)°. The γ angle deviates significantly from 90.0° (much more than the uncertainty in the measurement), whereas α and β do not, which means the tetragonal and trigonal space groups can be eliminated for the symmetry of this structure. Space group $Ibca$ can also be ruled out since it also requires right angles between axes in the body-centered setting. This means the only space groups possible based on the unit-cell parameters are $I\frac{2}{a}1\frac{2}{d}$ (unconventional setting for $Fddd$) and its subgroups (Figure 1). The reconstructed sections of the diffraction pattern along [001], [010] and $[1\bar{1}0]$ axes are shown in Figure 4. No reflections violating the body-centered lattice was detected. The systematic extinction of the *a*-glide plane is preserved in the *hk*0 section (Figure 4*a*), but not in the *h*0*l* section (Figure 4*c*) as the symmetry operation in this direction is not allowed by the γ angle. The 0*kl* section is identical to the *h*0*l* section (Figure S6*a*). Only reflections with $h+k+l$ = 4n are present in the *hhl* section (Figure 4*d*), indicating the *d*-glide plane along the diagonal (x, x, z) is also preserved. The $h\bar{h}l$ section shows the same systematic extinction following the *d*-glide symmetry, whereas the *hkh* section shows no such extinction (Figure S6*b*, *c*). These systematic extinctions in the diffraction pattern clearly show that the structure has a space group symmetry of $I\frac{2}{a}1\frac{2}{d}$ ($Fddd$). The diffraction pattern is overall very clean, and no splitting of reflections was observed even at high Bragg angles. No merohedral twinning is possible for this centrosymmetric orthorhombic symmetry, and the deviation from cubic symmetry (γ angle) is large enough for any pseudo-merohedral twinning to be easily detected during the crystal screening. Therefore, it is clear that the diffraction pattern is collected from a well-ordered single crystal of orthorhombic garnet.

The reflection intensity statistics further support an orthorhombic $I\frac{2}{a}1\frac{2}{d}$ symmetry. The R_{int} values for different space groups on the $I\frac{2}{a}1\frac{2}{d}$ branch in Figure 1 are listed in Table 3. The R_{int} value dramatically drop tetragonal $I\frac{4_1}{a}1\frac{2}{d}$ to orthorhombic $I\frac{2}{a}1\frac{2}{d}$ symmetry. However, the improvement of the R_{int} value for space groups lower than $I\frac{2}{a}1\frac{2}{d}$ is marginal. The 12 "observed" reflections violating the systematic extinction condition of the $I\frac{2}{a}1\frac{2}{d}$ space group (Table 3) are all at low diffraction angles with very weak intensities ($I < 5\sigma$), and none of them are visible in the raw diffraction data (Figure 4). Note that this is the first time a garnet structure shows unambiguous orthorhombic symmetry with clear systematic extinctions. Most previous reports of orthorhombic garnet structures used a monoclinic setting with ***b***-axis as the unique axis, presumably to save the trouble from lattice transformation when going to the monoclinic subgroup. However, there are 2 possible monoclinic subgroups of the orthorhombic $I\frac{2}{a}1\frac{2}{d}$ space group (Figure 1), with no particular reason for ***b***-axis being unique. Therefore, ***c***-axis should be the unique axis by default, considering two of the axes (***a*** and ***b***) are symmetrically equivalent in the body-centered cell setting. Making ***c***-axis the unique axis with $a = b$ and $\gamma > 90°$ is also consistent with the subgroup relation ($I\frac{4_1}{a}\bar{3}\frac{2}{d} \rightarrow I\frac{4_1}{a}1\frac{2}{d} \rightarrow I\frac{2}{a}1\frac{2}{d}$) as shown in Figure 1, following the unconventional subgroup symbols listed in International Table of Crystallography Volume A (Hahn 2002).

The structure solution and refinement of the orthorhombic garnet is straightforward. A structure solution could be reached easily using the charge flipping method, with Ca and Si assigned to the cube-like (8-coordinated) sites and tetrahedral sites respectively. Fe and Al are assigned to the larger and smaller Y site (Y_1 and Y_2 with Wyckoff letter 8*c* and 8*d*) respectively, and all the anion sites are assigned with O. After the initial convergence of the refinement, partial occupancies of Al and Fe are assigned to the Y_1 and Y_2 sites to account for the partial disordering in the structure, with the total occupancy of each site constrained to 1. Occupancies of the two Si sites are also relaxed to account for $(OH, F)_4$ substitution. The isotropic atomic displacement parameters (ADPs) are relaxed to harmonic ADPs for every atom in the structure in the last step, with the ADPs of Fe and Al in the same Y sites constrained to be identical. The final structure is checked to make sure there is no significant residual electron density, and all the

atoms have positive definite ADPs. All the atoms are refined as neutral atoms using the form factors from International Table Vol C tables 4.2.6.8 and 6.1.1.1. The chemical formula of the final refined structure is $Ca_3(Fe_{0.804}Al_{0.196})(Al_{0.779}Fe_{0.221})Si_{2.917}\square_{0.083})O_{12}$, which is very close to the composition from the EPMA analyses. Using the form factors of charged ions would result in a composition further from the EPMA analysis. Fe or Mn in the X sites and F in the anion sites are not considered in the refinement for simplicity, as disordering in every site of the structure would cause instability in the refinement. The slightly lower Fe and Si concentration compared to the EPMA analyses result can be explained by the anion sites only occupied by O in the refinement. If F is introduced to the anion sites, increasing the average electron density in the structure (larger scale parameter), the electron density of the cation sites would also increase accordingly, resulting in higher Fe and Si occupancies with a composition closer to the EPMA results.

The asymmetric unit of the refined structure is illustrated in Figure 5. The atom coordinates of the structure in the body-centered pseudo-cubic cell with $I\frac{2}{a}1\frac{2}{d}$ symmetry are provided in Table 4, along with the anisotropic temperature parameters (ADPs) of each atom in Table 5. The complete crystallographic information is provided in the Supplementary Material [data block I of Crystallographic Information File (CIF)], along with the same structure based on the conventional *Fddd* setting using the transformation ***a' = a + b, b' = b - a, c' = c*** (transformation matrix 1,1,0; -1,1,0; 0,0,1) (data block II). The crystal structure of the same crystal at 100K is also provided in the CIF file (data block III). Note that the reported structure in this paper (Table 2, 4 and 5) is refined against symmetry averaged intensities without absorption correction (data blocks I – III) to avoid artifacts from data processing, the result of which is even slightly better than the symmetry-averaged absorption-corrected data. This means that simply averaging the symmetry equivalent peaks with highly redundant data is quite effective at correcting the errors from the experiment (absorption corrected data is still better for refinement against unaveraged intensities). The statistics listed in Table 3, on the other hand, are from absorption-corrected intensities (with *SADABS* in *APEX3*) using multi-scan method in Laue group $\bar{1}$ (point group 1, so no symmetry bias is introduced from absorption correction). The structure refined against the unaveraged absorption-corrected intensities (15867 reflections total) is also provided in the CIF file (data block IV), in case the reader wants to perform symmetry or Hamilton tests on the

structure (Hamilton 1965). It is obvious that the symmetry loss is mainly due to the strong Fe-Al ordering in the Y site (an ordering parameter of ~0.8), which is responsible for the significant lattice distortion with $\gamma = 90.29(2)°$ (largest in all reported non-cubic garnets). Small but obvious difference in the tetrahedral site occupancies is also detected in the structure, indicating the (OH, F) substitution prefers the more symmetrical Si_2 site over Si_1. All the bond distances in the structure are listed in Table 6. The Y_1-O bonds are about 0.05 Å longer than the Y_2-O bonds. The relations between the Y-O bond lengths and the Fe occupancies are consistent with previously published results from Cr-rich ugrandite garnet (Shtukenberg et al. 2005). The Si-O bonds of the $(OH, F)_4$ preferred Si_2 site are about 0.01 Å longer than those of Si_1–O bonds.

Twinning and average structure of twinned garnet

Pseudo-merohedral twinning cannot be avoided in non-cubic garnets, no matter what mechanism is causing the cation ordering in the structure. However, there are no reported considerations about possible twins in "single-crystal" structural refinements. The strongly birefringent zone in the garnet sample is obviously twinned, as indicated by the fluctuations in the interference colors (Figure 2). A diffraction frame of a screened crystal showing obvious peak splitting from twinning is provided in Figure S7. It is hard to estimate the average twin domain size of the birefringent zone, but based on the crystal picked for the single-crystal XRD, the larger domains are at least a few hundred microns in diameter. The high-resolution TEM image in Figure 6 shows two twin domains smoothly transform into each other without an obvious boundary. The fast Fourier transform (FFT) patterns of the two regions show diffraction patterns of [100] and [001] zone-axes respectively, corresponding to the 0*kl* and *hk*0 sections of the X-ray diffraction pattern (Figure 4*a*,*c*). The lattice distortion of the sample in this study is large enough for any twinning to be easily detected, but a less ordered structure may have pseudo-merohedral twinning that is much harder to identify due to smaller deviation from cubic lattice. Powder X-ray diffraction is one way to bypass the problem introduced by twinning, which is used by several previous structural studies of anisotropic garnet (Kingma and Downs 1989; Antao 2013a, b, 2021a, b; Antao and Klincker 2013; Antao et al. 2015; Tančić et al. 2020). The powder diffraction pattern of the birefringent zone of the garnet is shown in Figure 7. The diffraction pattern seems overall very similar to a cubic garnet, as the peak splitting due to lattice distortion is impossible to resolve in a lab based powder X-ray diffractometer. However, some reflections

This is the peer-reviewed, final accepted version for American Mineralogist, published by the Mineralogical Society of America.
The published version is subject to change. Cite as Authors (Year) Title. American Mineralogist, in press.
DOI: https://doi.org/10.2138/am-2022-8455. http://www.minsocam.org/

violating the $Ia\bar{3}d$ symmetry (i.e. 101, 103, 303) can be clearly seen in the diffraction pattern, which has not been observed in any previous studies. Diffraction peaks from powder XRD of the orthorhombic garnet are listed in Table S1.

Lowering in symmetry (or dissymmetrization) from cubic $Ia\bar{3}d$ to orthorhombic $I\frac{2}{a}1\frac{2}{d}$ would give rise to 6 possible different orientations, each of which corresponds to one possible pseudo-merohedral twin domain. Two distinct twin operations are required to generate all 6 orientations, namely {010} *a*-glide and {101} *d*-glide, which are the glide symmetries lost from the $Ia\bar{3}d \rightarrow I\frac{2}{a}1\frac{2}{d}$ transformation. Note that twinning by rotational operations (i.e., 2-fold around ⟨101⟩, 3-fold around ⟨111⟩/⟨1$\bar{1}$1⟩, and 4-fold around ⟨100⟩/⟨001⟩), in which the composition planes are parallel instead of perpendicular to the operation axes, would be technically different from twinning by glide-planes. Although in theory the exact twin operation may be deduced from the optical indicatrices across sharp twin boundaries [i.e., the crystals reported by Hariya and Kimura (1978), Akizuki (1984) and Jamtveit (1991)], they are not distinguishable from the diffraction pattern, especially when the distortion from cubic lattice is very small. The 6 different orientations (twin domains) can be labeled TDoo, TDo*d*, TDo*d*', TD*a*o, TD*ad*, TD*ad*' following the symmetry relations among one another, as illustrated in Figure 8 [i.e. TDoo is related to TDo*d* by a (101)-glide, and to TD*ad*' by a (100)-glide plus a (011)-glide].

A twinned orthorhombic garnet crystal may contain domains of all 6 different orientations with different proportions. Any two twin domains related by {101} *d*-glide operation would create reflections violating the extinction conditions of $I\frac{2}{a}1\frac{2}{d}$ space group, resulting in a triclinic symmetry for the diffraction pattern. Reducing the symmetry from $I\frac{2}{a}1\frac{2}{d}$ to $I\bar{1}$ would differentiate each Y site into four symmetrically different sites (Shtukenberg et al. 2005), which are labeled for TDoo in Figure 8. All the possible twin domains have the same topology and only the position of Al and Fe are swapped in a certain way from one another (Figure 8). Therefore, if an $I\bar{1}$ structure is refined against a twinned diffraction pattern of an orthorhombic garnet, the result would be a weighted average of the 6 possible orientations. Assuming the relative proportion of each twin domain in a twinned crystal is t_{oo}, t_{od}, $t_{od'}$, t_{ao}, t_{ad} and $t_{ad'}$ respectively, the corresponding Fe occupancy in each Y site of the corresponding $I\bar{1}$ structure would be:

$$Fe_{Y1\_1} = Fe_{Y1\_3} = (t_{oo} + t_{od} + t_{od'})Fe_{Y1} + (t_{ao} + t_{ad} + t_{ad'})Fe_{Y2}$$

This is the peer-reviewed, final accepted version for American Mineralogist, published by the Mineralogical Society of America.
The published version is subject to change. Cite as Authors (Year) Title. American Mineralogist, in press.
DOI: https://doi.org/10.2138/am-2022-8455. http://www.minsocam.org/

$$Fe_{Y1\_2} = Fe_{Y1\_4} = (t_{oo} + t_{ad} + t_{ad'})Fe_{Y1} + (t_{ao} + t_{od} + t_{od'})Fe_{Y2}$$

$$Fe_{Y2\_1} = Fe_{Y2\_4} = (t_{ao} + t_{ad} + t_{od'})Fe_{Y1} + (t_{oo} + t_{od} + t_{ad'})Fe_{Y2}$$

$$Fe_{Y2\_2} = Fe_{Y2\_3} = (t_{ao} + t_{od} + t_{ad'})Fe_{Y1} + (t_{oo} + t_{ad} + t_{od'})Fe_{Y2}$$

Note that the refined structure is not an exact average because the intensity of a certain reflection from a single crystal is proportional to the square of the structure factor. Nonetheless, the unusual pattern shown in the equations above is expected for the $I\bar{1}$ structure refined from a twinned orthorhombic data set, where pairs of Y sites that are not symmetrically equivalent have the same occupancies. This is observed in almost all of the previously published $I\bar{1}$ structures (Takéuchi et al. 1982; Kingma and Downs 1989; Wildner and Andrut 2001; Shtukenberg et al. 2005; Frank-Kamenetskaya et al. 2007). Hatch and Griffen (1989) first noticed this phenomenon in the $I\bar{1}$ garnet structure reported by Takéuchi et al. (1982), but misinterpreted this as a single order parameter in different orientations, instead of twinning. The Landau theory (based on group theory of the $Ia\bar{3}d$ space group) used by Hatch and Griffen (1989) only applies to the temperatures close to the phase transition, whereas the studied $I\bar{1}$ structures are supposedly ordered further at much lower temperatures, therefore has no constraints to preserve this special pattern. We have simulated a series of twinned diffraction data of the orthorhombic garnet structure and used them to refine structures in the $I\bar{1}$ space group. The results are provided in the Appendix, which demonstrate different ordering patterns can indeed result from twinning.

It should be noted that twinning by (100) glide plane flips all the Y_1 sites to Y_2 sites (and vice versa), with the orientations of all the symmetry elements unchanged (Figure 8). This means a crystal with only (100) glide twins would still show an $I\frac{2}{a}1\frac{2}{d}$ space group in the symmetry test, but the Fe/Al occupancies would be averaged out between Y_1 and Y_2 sites, resulting in a smaller order parameter. The (OH, F) ordering in the Si sites, however, would be preserved, as they remain in the same positions after this twin operation. This also means the only pseudo-monoclinic symmetry that can be created by averaging different twin domains is $I11\frac{2}{d}$, and monoclinic structures of $I\,{}^{2}/_{a}$ space group can only be created by further ordering (Figure 1 and Appendix).

DISCUSSIONS

The main reason causing the ambiguity of the cation ordering mechanism for the anisotropic grandite garnet is the large variety of different structures reported. The heterogeneity often observed in these birefringent garnet crystals also make the case more complicated. There are obviously many different factors controlling the final appearance and ordering states of the grandite garnet, including growth kinetics and thermodynamics of the solid solution. The structure reported in this paper shows an unambiguous orthorhombic symmetry, with much stronger Fe/Al ordering between two Y sites than any previously reported garnet structures. The composition very close to the ideal stoichiometry of a perfectly ordered structure $Adr_{50}Grs_{50}$ also strongly suggest a thermodynamically stable phase exist for intermediate compositions in the solid solution at low temperature. A schematic phase diagram of the grossular-andradite solid solution is presented in Figure 9 based on the studied garnets and previously reported garnets with known temperature range by Jamtveit (1991).

Growth kinetics of garnet plays an important role in the formation of birefringent garnet, as evident by the zoning and sector twining that are often observed (Hariya and Kimura 1978; Akizuki 1984; Jamtveit 1991), and may affect the cation ordering in the structure as many studies suggested (Callen 1971; Gali 1983; Akizuki 1984; Shtukenberg et al. 2001, 2005; Frank-Kamenetskaya et al. 2007). However, the "growth dissymmetrization" phenomenon is mostly theoretical with no direct evidences, and kinetics is mostly known to favor the growth of disordered instead of ordered structures under metastable conditions (Carpenter and Putnis 1985; Pollok et al. 2001). It is not possible for a strongly ordered orthorhombic structure to be created only from the "growth dissymmetrization". Most models for growth-induced ordering predicts an $I\bar{1}$ structure (Shtukenberg et al. 2005; Frank-Kamenetskaya et al. 2007), and growth normal to {110} planes that is required to create orthorhombic symmetry (Gali 1983) should create perfectly oriented domains relative to the growth surface, instead of the randomly twinned domains as observed in the sample studied in this paper (Figures 2 and 6). The large order parameter (~0.8) of the structure studied in this paper also cannot be explained by growth kinetics. As demonstrated in the previous section, pseudo-merohedral twinning can create all different kinds of pseudo-symmetry, which none of the previous structure studies have considered in their refinements. It is most likely that the large varieties of different non-cubic

structures are results of twinned crystals of different domain proportions. It needs to be noted that the orthorhombic symmetry is only expected for Y site ordering, and ordering in the X or Z sites could result in different subgroup symmetries [i.e. tetragonal for X site ordering (Griffen et al. 1992; Cesare et al. 2019) and trigonal for Z site ordering (Krivovichev et al. 2021)], which are easily distinguishable based on chemical analysis. Moreover, submicron chemical zoning and intergrowths are very common in anisotropic garnets (Ingerson and Barksdale 1943; Akizuki et al. 1984; Hainschwang and Notari 2006; Antao 2013b; Nakamura et al. 2017), which means some of the previously reported structures may not even be from a single homogeneous phase. Note that the symmetry can be conclusively determined in this paper in a twin-free crystal only because the ordering is strong enough to significantly distort the lattice from cubic symmetry. In a less ordered and more densely twinned crystal, the lattice with strained twin boundaries can easily show metrically cubic symmetry, similar to the effect observed in micro-tweed structure of orthoclase with metrically monoclinic lattice (Eggleton and Buseck 1980; Xu et al., 2019).

The strongest evidence for the thermodynamic stability of orthorhombic garnet structure for intermediate compositions at low temperature (Figure 9) comes from the oscillatory growth zoning between ~Adr_{100} (pure andradite) and ~$Adr_{53}Grs_{47}$ with particularly consistent compositions and sharp boundaries (Figure 2). The same phenomena have been reported by in garnet from Colorado, Thera Island (Aegean Sea), and southern Norway (Lessing and Standish 1973; Murad 1976; Jamtveit et al. 1993, 1995; Pollok et al. 2001). Similar phenomena between ~$Adr_{10}Grs_{90}$ and ~$Adr_{50}Grs_{50}$, as well as coexisting unzoned isotropic and anisotropic grandite garnets in skarn zones around hydrothermal veins, have also been reported in other birefringent garnets (see Jamtveit 1991). This indicates the presence of a miscibility gap between ~Adr_{100} and ~$Adr_{50}Grs_{50}$ (also between ~Adr_0 and ~Adr_{50}) at low temperature in the solid solution series (Figure 9). The lamellar intergrowths observed by Hirai and Nakazawa (1986), which are interpreted as exsolution textures also indicate immiscibility for certain compositions. Note that thermodynamic stability of the orthorhombic garnet phase means birefringent garnet can be formed by both direct growth at low temperature and through phase transformation during cooling, which is consistent with the various zoning and textures observed in natural and synthetic garnets. Jamtveit (1991) successfully models the oscillatory zoning pattern by considering the miscibility gaps in the solid solution using the theory of nonlinear dynamics. The ordered orthorhombic structure perfectly explains the presence of the miscibility gaps in the solid

solution (Figure 9), where the Gibbs free energy is dramatically decreased for intermediate grandite through Fe/Al ordering, driving the phase separation between intermediate grandite and pure end members. It is possible that the periodic lamellar intergrowth/zoning found in iridescent garnet (Ingerson and Barksdale 1943; Akizuki et al. 1984; Hainschwang and Notari 2006; Nakamura et al. 2017) could also be formed during oscillatory growth suggested by Jamtveit (1991).

Thermal information of previously reported anisotropic garnet structures are very limited, making it difficult to constrain the shapes of the miscibility gaps in the phase diagram (Figure 9). The fluid inclusions trapped in the garnet, along with the chemical composition of different zones in the garnet studied in this paper, shows that the miscibility gap is almost at its widest at ~200 °C. Grandite with compositions of ~$Adr_{95}Grs_5$ and ~$Adr_{65}Grs_{35}$ were found coexisting in the skarn (sample R8923) at ~400 °C by Jamtveit (1991), which indicates the miscibility gap is asymmetrical tilting towards the andradite end member, instead of the shape from molecular simulation by Becker and Pollok (2002). Similar compositional gap (between ~$Grs_{65}Adr_{35}$ and ~$Grs_{90}Adr_{10}$) was reported in the grossular-rich side (Engi and Wersin, 1987). Garnet crystals from skarn deposits have documented homogenization temperatures of fluid inclusions that range from ~ 400°C to ~150°C (Boni et al. 1990), which means all the garnets found in skarn with intermediate compositions are at least partially ordered. Optical anisotropy can be recreated from an isotropic natural grandite (heated) with composition of ~$Adr_{90}Grs_{10}$ at 600°C (Hariya and Kimura 1978), but synthetic grandite shows an isotropic/anisotropic transition at much lower temperature. It should be noted that the ordering kinetics of cations in the garnet structure is poorly understood. The Al/Si ordering rate in feldspar structures are known to change dramatically with the amount of H_2O in the composition (Yund and Tullis 1980). Therefore, a large variation in the cation ordering rate in garnet may be expected considering the wide range of (OH) content that can be incorporated into the structure.

The residual strain caused by lattice discrepancy in chemically zoned garnet has been proposed to produce birefringence (Akizuki 1984; Hirai and Nakazawa 1986; Antao and Klincker 2013). However, the pure andradite zone in the sample studied in this paper shows no observable optical anomaly, despite the sharp boundaries with the orthorhombic grandite with drastically different composition (~$Adr_{53}Grs_{47}$). Stress-induced birefringence is expected to be very low in garnets

(Lynch et al. 1973), and dissipates quickly away from the strained interface, as shown by the birefringent halos around zircon and coesite inclusions in garnets (Campomenosi et al. 2018). None of the previously reported anisotropic garnet crystals are pure end member, which means it is likely that cation ordering is at least partially involved in all observed optical anomalies in grandite garnet. Reported garnets with high birefringence (~ 0.010) all have compositions close to $Adr_{50}Grs_{50}$ (Mariko and Nagai 1980; Hirai and Nakazawa 1986; Frank-Kamenetskaya et al. 2007), and the birefringence vs composition plots (Mariko and Nagai 1980; Shtukenberg et al. 2001) show that the higher the birefringence, the closer the composition is to the middle of the solid solution. Theoretical calculation using a quantum mechanical approach indicates that a fully ordered structure with composition of $Adr_{50}Grs_{50}$ has the highest birefringence ($\delta = 0.023$) (Lacivita et al. 2013), which is consistent with the observed birefringence ($\delta \sim 0.021$) of the orthorhombic garnet in this paper.

IMPLICATIONS

The crystal structures and ordering states of natural birefringent garnet crystals are thermodynamically controlled, which can record information regarding the cooling history of the host rock. The textures observed in anisotropic garnet can also be twin domains or even exsolution lamellae from solid state phase transitions, instead of just growth features recording the crystallization condition as suggested by the "growth dissymmetrization" theory. The phase diagram of the grossular-andradite solid solution should be studied in detail to better constrain the shapes and positions of the miscibility gaps between the orthorhombic and the cubic (pure end members) phases, which may potentially be used as geothermometer and/or geobarometer. Based on the reported structure of uvarovite, it is very likely that the uvarovite-grossular solid solution has a similar phase relation with orthorhombic Cr/Al ordering for intermediate compositions at low temperature. The solvi between orthorhombic Al-Cr garnet and its end-members (grossular & uvarovite) will be narrower than the solvi in the grossular-andradite system (Figure S8), because the difference between Al^{3+} and Cr^{3+} is smaller than the difference between Al^{3+} and Fe^{3+} in their ionic radii and chemical hardness (Xu et al. 2017).

Most of the previously reported non-cubic garnet structures, especially those with $I\bar{1}$ space group symmetry, are most likely from twinned orthorhombic crystals, potentially also containing

intergrowth of more than one phase with different compositions. These structures should be revisited to better evaluate their structures and ordering states. The conclusions made based on triclinic (pseudo-)symmetry should be cited with immense caution. Future studies of anisotropic garnet structures should carefully take potential twinning into consideration during the refinement. Structure studies of garnet with powder XRD, although bypassing the twinning problem, miss important information to determine the correct symmetry due to significant peak overlapping, therefore powder XRD is not reliable when used by itself. Combination of single-crystal diffraction and high-resolution TEM, plus selected-area electron diffraction (SAED), as demonstrated in previous study (Jin et al. 2018), is the most reliable method for determining crystal structures with pseudo-symmetry. Careful examination of raw single-crystal diffraction data is critical, rather than simply following the automated data reduction procedure in the programs, especially when studying crystals with potential twinning and pseudo-symmetry.

ACKNOWLEDGMENT

Authors thank Professor Charles Geiger and two anonymous reviewers for their critical reviews and constructive comments. This study was partially supported by National Science Foundation (grant No. EAR-1530614).

REFERENCES

Akizuki, M. (1984) Origin of optical variations in grossular-andradite garnet. American Mineralogist, 69, 328–338.

——— (1989) Growth structure and crystal symmetry of grossular garnets from the Jeffrey Mine, Asbestos, Quebec, Canada. American Mineralogist, 74, 859–864.

Akizuki, M., Nakai, H., and Suzuki, T. (1984) Origin of iridescence in grandite garnet. American Mineralogist, 69, 896–901.

Allen, F.M., and Buseck, P.R. (1988) XRD, FTIR, and TEM studies of optically anisotropic grossular garnets. American Mineralogist, 73, 568–584.

Andrut, M., and Wildner, M. (2001) The crystal chemistry of birefringent natural uvarovites: Part I. Optical investigations and UV-VIS-IR absorption spectroscopy. American Mineralogist, 86, 1219–1230.

Andrut, M., and Wildner, M. (2002) The crystal chemistry of birefringent natural uvarovites. Part III. Application of the superposition model of crystal fields with a characterization of synthetic cubic uvarovite. Physics and Chemistry of Minerals, 29, 595–608.

Andrut, M., Wildner, M., and Beran, A. (2002) The crystal chemistry of birefringent natural uvarovites. Part IV. OH defect incorporation mechanisms in non-cubic garnets derived from polarized IR spectroscopy. European Journal of Mineralogy, 14, 1019–1026.

Antao, S.M. (2013a) The mystery of birefringent garnet: is the symmetry lower than cubic? Powder Diffraction, 28, 281–288.

——— (2013b) Three cubic phases intergrown in a birefringent andradite-grossular garnet and their implications. Physics and Chemistry of Minerals, 40, 705–716.

——— (2021a) Crystal Chemistry of Six Grossular Garnet Samples from Different Well-Known Localities. Minerals, 11, 767.

——— (2021b) Crystal Structure of an Anisotropic Pyrope Garnet That Contains Two Cubic Phases. Minerals, 11, 1320.

Antao, S.M., and Klincker, A.M. (2013) Origin of birefringence in andradite from Arizona, Madagascar, and Iran. Physics and Chemistry of Minerals, 40, 575–586.

Antao, S.M., Zaman, M., Gontijo, V.L., Camargo, E.S., and Marr, R.A. (2015) Optical anisotropy, zoning, and coexistence of two cubic phases in andradites from Quebec and New York. Contributions to Mineralogy and Petrology, 169, 10.

Anthony, J.W., Williams, S.A., Bideaux, R.A., and Grant, R.W. (1995) Mineralogy of Arizona, 3rd ed., 527 p. (W.E. Wilson, Ed.). University of Arizona Press, Tucson, Arizona, USA.

Badar, M.A., Hussain, S., Niaz, S., and Rehman, S.U. (2016) Anomalous optical variations in the grossular garnet from the Eden Mills, Belvidere Mountain (Vermont, USA). Arabian Journal of Geosciences, 9, 1–9.

Becker, U., and Pollok, K. (2002) Molecular simulations of interfacial and thermodynamic mixing properties of grossular–andradite garnets. Physics and Chemistry of Minerals, 29, 52–64.

Blanc, Y., and Maisonneuve, J. (1973) Sur la biréfringence des grenats calciques. Bulletin de Minéralogie, 96, 320–321.

Bodnar, R.J. (1994) Interpretation of microthermometric data for H_2O-NaCl fluid inclusions. in. In Fluid Inclusions in Minerals: Methods and Applications pp. 117–130.

Boni, M., Rankin, A.H., and Salvadori, M. (1990) Fluid inclusion evidence for the development of Zn–Pb–Cu–F skarn mineralization in SW Sardinia, Italy. Mineralogical Magazine, 54, 279–287.

Callen, H. (1971) Growth-induced anisotropy by preferential site ordering in garnet crystals. Applied Physics Letters, 18, 311–313.

Campomenosi, N., Mazzucchelli, M.L., Mihailova, B., Scambelluri, M., Angel, R.J., Nestola, F., Reali, A., and Alvaro, M. (2018) How geometry and anisotropy affect residual strain in host-inclusion systems: Coupling experimental and numerical approaches. American Mineralogist, 103, 2032–2035.

Carpenter, M.A., and Putnis, A. (1985) Cation Order and Disorder during Crystal Growth: Some Implications for Natural Mineral Assemblages. In A.B. Thompson and D.C. Rubie, Eds., Metamorphic Reactions: Kinetics, Textures, and Deformation Vol. 4, pp. 1–26. Springer, New York, NY.

Cesare, B., Nestola, F., Johnson, T., Mugnaioli, E., Della Ventura, G., Peruzzo, L., Bartoli, O., Viti, C., and Erickson, T. (2019) Garnet, the archetypal cubic mineral, grows tetragonal. Scientific Reports, 9, 14672.

Chase, A.B., and Lefever, R.A. (1960) Birefringence of synthetic garnets. American Mineralogist, 45, 1126–1129.

Deer, W.A., Howie, R.A., and Zussman, J. (1982) Rock-Forming Minerals: Orthosilicates, Volume 1A, 2nd ed., 940 p. Vol. 1A. Geological Society of London, London, United Kingdom.

Eggleton, R.A., and Buseck, P.R. (1980) The orthoclase-microcline inversion: A high-resolution transmission electron microscope study and strain analysis. Contributions to Mineralogy and Petrology, 74, 123–133.

Engi, M., and Wersin, P. (1987) Derivation and application of solution model for calcic garnet. Schweizerische Mineralogische und Petrographische Mitteilungen, 67, 53-73.

Foord, E.E., and Mills, B.A. (1978) Biaxiality in "isometric" and "dimetric" crystals. American Mineralogist, 63, 316–325.

Frank-Kamenetskaya, O.V., Rozhdestvenskaya, I.V., Shtukenberg, A.G., Bannova, and Skalkina, Y.A. (2007) Dissymmetrization of crystal structures of grossular-andradite garnets $Ca_3(Al,Fe)_2(SiO_4)_3$. Structural Chemistry, 18, 493–503.

Gali, S. (1983) Grandite garnet structures in connection with the growth mechanism. Zeitschrift für Kristallographie - Crystalline Materials, 163, 43–52.

Gali, S. (1984) Reduction of symmetry in grandite solid solution. Acta Geologica Hispanica, 19, 287–293.

Geiger, C.A. (2008) Silicate garnet: A micro to macroscopic (re)view. American Mineralogist, 93, 360–372

——— (2016) A tale of two garnets: The role of solid solution in the development toward a modern mineralogy. American Mineralogist, 101, 1735-1749.

Geiger, C.A., and Rossman, G.R. (2018) IR spectroscopy and OH- in silicate garnet: The long quest to document the hydrogarnet substitution. American Mineralogist, 103, 384–393.

——— (2020) Nano-size hydrogarnet clusters and proton ordering in calcium silicate garnet: Part I. The quest to understand the nature of "water" in garnet continues. American Mineralogist, 105, 455–467.

Grew, E.S., Locock, A.J., Mills, S.J., Galuskina, I.O., Galuskin, E.V., and Hålenius, U. (2013) Nomenclature of the garnet supergroup. American Mineralogist, 98, 785–811.

Griffen, D.T., Hatch, D.M., Phillips, W.R., and Kulaksiz, S. (1992) Crystal chemistry and symmetry of a birefringent tetragonal pyralspite$_{75}$-grandite$_{25}$ garnet. American Mineralogist, 77, 399–406.

Hahn, Th. (2002) The 230 space groups. In Th. Hahn, Ed., International Tables for Crystallography Volume A: Space-group symmetry, pp. 112–717. Springer Netherlands, Dordrecht.

Hainschwang, T., and Notari, F. (2006) The cause of iridescence in rainbow andradite from Nara, Japan. Gems & Gemology, 42, 248–258.

Hamilton, W.C. (1965) Significance tests on the crystallographic R factor. Acta Crystallographica, 18, 502–510.

Hariya, Y., and Kimura, M. (1978) Optical anomaly garnet and its stability field at high pressures and temperatures. Journal of the Faculty of Science, Hokkaido University, 18, 611–624.

Hatch, D.M., and Griffen, D.T. (1989) Phase transitions in the grandite garnets. American Mineralogist, 74, 151–159.

Hirai, H., and Nakazawa, H. (1986) Visualizing low symmetry of a grandite garnet on precession photographs. American Mineralogist, 71, 1210–1213.

Hurai, V., Huraiová, M., Slobodník, M., and Thomas, R. (2015) Chapter 5 - Interpretation of Microthermometric Data. In V. Hurai, M. Huraiová, M. Slobodník, and R. Thomas, Eds., Geofluids pp. 117–170. Elsevier.

Ingerson, E., and Barksdale, J.D. (1943) Iridescent garnet from the Adelaide Mining District, Nevada. American Mineralogist, 28, 303–312.

Jamtveit, B. (1991) Oscillatory zonation patterns in hydrothermal grossular-andradite garnet: Nonlinear dynamics in regions of immiscibility. American Mineralogist, 76, 1319–1327.

Jamtveit, B., Wogelius, R.A., and Fraser, D.G. (1993) Zonation patterns of skarn garnets: Records of hydrothermal system evolution. Geology, 21, 113–116.

Jamtveit, B., Ragnarsdottir, K.V., and Wood, B.J. (1995) On the origin of zoned grossular-andradite garnets in hydrothermal systems. European Journal of Mineralogy, 7, 1399–1410.

Jin, S., Xu, H., Lee, S., and Fu, P. (2018) Jinshajiangite: structure, twinning and pseudo-symmetry. Acta Crystallographica Section B, 74, 325–336.

Kingma, K.J., and Downs, J.W. (1989) Crystal-structure analysis of a birefringent andradite. American Mineralogist, 74, 1307–1316.

Kobayashi, S., Miyawaki, R., Momma, K., Fujisawa, A., and Kaneda, H. (2013) Anisotropic garnet from the Yamansu ore deposit, Xinjiang, China. Journal of Mineralogical and Petrological Sciences, 108, 245–254.

Krivovichev, S.V., Panikorovskii, T.L., Yakovenchuk, V.N., Selivanova, E.A., and Ivanyuk, G.Y. (2021) Trigonal variation in the garnet supergroup: the crystal structure of nikmelnikovite, $Ca_{12}Fe^{2+}Fe^{3+}{}_3Al_3(SiO_4)_6(OH)_{20}$, from Kovdor massif, Kola Peninsula, Russia. Mineralogical Magazine, 85, 620–626.

Lacivita, V., D'Arco, P., Orlando, R., Dovesi, R., and Meyer, A. (2013) Anomalous birefringence in andradite–grossular solid solutions: a quantum-mechanical approach. Physics and Chemistry of Minerals, 40, 781–788.

Lager, G.A., Armbruster, T., Rotella, F.J., and Rossman, G.R. (1989) OH substitution in garnets; X-ray and neutron diffraction, infrared, and geometric-modeling studies. American Mineralogist, 74, 840–851.

Lessing, P., and Standish, R.P. (1973) Zoned Garnet from Crested Butte, Colorado. American Mineralogist, 58, 840–842.Manning, C. E., and Bird, D. K. (1990) Fluorian garnets from

the host rocks of the Skaergaard intrusion: Implications for metamorphic fluid composition. American Mineralogist, 75, 859-873.

Lynch, R.T., Dillon, J.F., and Van Uitert, L.G. (1973) Stress birefringence in ferrimagnetic garnets. Journal of Applied Physics, 44, 225–229.

Mariko, T., and Nagai, Y. (1980) Birefringence and composition of grandite garnet from the Shinyama ore deposit of the Kamaishi mine, Iwate Prefecture, Japan. Mineralogical Journal, 10, 181–191.

Momma, K., and Izumi, F. (2011) VESTA 3 for three-dimensional visualization of crystal, volumetric and morphology data. Journal of Applied Crystallography, 44, 1272–1276.

Murad, E. (1976) Zoned, birefringent garnets from Thera Island, Santorini Group (Aegean Sea). Mineralogical Magazine, 40, 715–719.

Myers, G.L. (1994) Geology of the Copper Canyon-Fortitude skarn system, Battle Mountain, Nevada. Ph.D., Washington State University, Pullman, Washington.

Nakamura, Y., Kuribayashi, T., and Nagase, T. (2016) Cation ordering of {110} and {211} sectors in grandite garnet from Mali. Journal of Mineralogical and Petrological Sciences, 111, 385–397.

Nakamura, Y., Kuribayashi, T., Nagase, T., and Imai, H. (2017) Cation ordering in iridescent garnet from Tenkawa village, Nara prefecture, Japan. Journal of Mineralogical and Petrological Sciences, 112, 97–101.

Petříček, V., Dušek, M., and Palatinus, L. (2014) Crystallographic Computing System JANA2006: General features. Zeitschrift für Kristallographie-Crystalline Materials, 229, 345–352.

Pollok, K., Jamtveit, B., and Putnis, A. (2001) Analytical transmission electron microscopy of oscillatory zoned grandite garnets. Contributions to Mineralogy and Petrology, 141, 358–366.

Ross, C.P. (1925) Geology and ore deposits of the Aravaipa and Stanley mining districts, Graham County, Arizona. Bulletin. Govt. Print. Off.,.

Rossman, G.R., and Aines, R.D. (1986) Spectroscopy of a birefringent grossular from Asbestos, Quebec, Canada. American Mineralogist, 71, 779–780.

Rossmanith, E., and Armbruster, T. (1995) The intensity of forbidden reflections of pyrope: Umweganregung or symmetry reduction? Zeitschrift für Kristallographie - Crystalline Materials, 210, 645–649.

Shtukenberg, A.G., Punin, Y.O., Frank-Kamenetskaya, O.V., Kovalev, O.G., and Sokolov, P.B. (2001) On the origin of anomalous birefringence in grandite garnets. Mineralogical Magazine, 65, 445–459.

Shtukenberg, A.G., Popov, D.Y., and Punin, Y.O. (2002) An application of the point-dipole model to the problem of optical anomalies in grandite garnets. Mineralogical Magazine, 66, 275–286.

Shtukenberg, A.G., Popov, D.Y., and Punin, Y.O. (2005) Growth ordering and anomalous birefringence in ugrandite garnets. Mineralogical Magazine, 69, 537–550.

Takéuchi, Y., and Haga, N. (1976) Optical Anomaly and Structure of Silicate Garnets. Proceedings of the Japan Academy, 52, 228–231.

Takéuchi, Y., Haga, N., Umizu, S., and Sato, G. (1982) The derivative structure of silicate garnets in grandite. Zeitschrift für Kristallographie - Crystalline Materials, 158, 53–100.

Tančić, P., Kremenović, A., and Vulić, P. (2020) Structural dissymmetrization of optically anisotropic $Grs_{64\pm1}Adr_{36\pm1}Sps_2$ grandite from Meka Presedla (Kopaonik Mt., Serbia). Powder Diffraction, 35, 7–16.

Theodore, T.G., Howe, S.S., Blake, D.W., and Wotruba, P.R. (1986) Geochemical and fluid zonation in the skarn environment at the Tomboy—Minnie gold deposits, Lander County, Nevada. Journal of Geochemical Exploration, 25, 99–128.

Vanko, D.A., Bodnar, R.J., and Sterner, S.M. (1988) Synthetic fluid inclusions: VIII. Vapor-saturated halite solubility in part of the system $NaCl\text{-}CaCl_2\text{-}H_2O$, with application to fluid inclusions from oceanic hydrothermal systems. Geochimica et Cosmochimica Acta, 52, 2451–2456.

Warr, L.N. (2021) IMA–CNMNC approved mineral symbols. Mineralogical Magazine, 85, 291–320.

Wildner, M., and Andrut, M. (2001) The crystal chemistry of birefringent natural uvarovites: Part II. Single-crystal X-ray structures. American Mineralogist, 86, 1231–1251.

Xu, H., Xu, D.C., and Wang, Y. (2017) Natural Indices for the Chemical Hardness/Softness of Metal Cations and Ligands. ACS Omega, 2, 7185–7193.

Xu, H., Jin, S., Lee, S., and Hobbs, F.W.C (2019) Nano-phase $KNa(Si_6Al_2)O_{16}$ in adularia: A new member in the alkali feldspar series with ordered K–Na Distribution. Minerals, 9, 649.

Yund, R.A., and Tullis, J. (1980) The effect of water, pressure, and strain on Al-Si order-disorder kinetics in feldspar. Contributions to Mineralogy and Petrology, 72, 297–302.

Captions of figures

Figure 1. The centrosymmetric subgroup graph of the space group $Ia\bar{3}d$, along with the lattice parameter constraints and Wyckoff symbols of the X, Y, and Z sites in each space group. All the Hermann–Mauguin notations in the graph are based on the body-centered cubic setting (1st position-[001], 2nd position-[111], 3rd position-[110]), for easily comparing the symmetry elements among different space groups. Some unconventional space group symbols are created this way, with the corresponding conventional symbols in parenthesis. The unconventional settings are necessary in this case to differentiate the two distinct settings of the monoclinic subgroup *C*2/*c*. The multiplicity of each Wyckoff position may be different from the conventional space group setting due to changes in unit cell volumes (i.e., the $I\frac{2}{a}1\frac{2}{d}$ unit cell has half the volume of the conventional *Fddd* unit cell). The critical symmetry elements (4_1, 2/*a*, 2/*c*, 2/*d*, and 3) that are lost for each supergroup-subgroup relation is marked on the arrows (2/*c* is a symmetry in the [100] direction which is not explicit in the Hermann-Mauguin notation in cubic setting). Note that these unconventional space group symbols are used in the International Tables of Crystallography Volume A. for the "maximal non-isomorphic subgroups" (Hahn 2002).

Figure 2. Optical image (crossed polarizer) of a thin section cut perpendicular to [111] of cubic unit cell setting (a) and back-scattering electron microscopic image (high resolution image provided in Figure S3) (b) from lower part area of image (a) showing oscillatory zoning between orthorhombic garnet and andradite. Optical image (crossed polarizer) of a thin section (50 μm thick) cut perpendicular to ~***b***-axis (c) and back-scattering electron microscopic image (d) showing oscillatory zoning between orthorhombic garnet and andradite. The crystal also displays sector twinning. Heterogeneous interference colours in the orthorhombic garnet layers result from domains with different orientations in twin relationships. The areas with uniform highest interference colour (second order red here, see areas inside white circles) were selected for single-crystal XRD work. See Figure S4 in the supplementary material for the cutting planes / positions in the ideal {110} garnet shape for the two thin sections.

Figure 3. Photomicrographs of fluid inclusions inside the oscillatory andradite and orthorhombic garnet zone during microthermometry. V = vapor, L = liquid, T_h = homogenization temperature, T_f = freezing temperature of liquid phase, and T_m = melting temperature of ice.

Figure 4. Reconstructed sections of the X-ray diffraction data showing symmetry elements through systematic extinctions. The remaining mirror planes (*d*-glide in real space) and associated extinctions are marked with dash lines and dash circles.

Figure 5. The asymmetric unit of the orthorhombic garnet structure projected along ***a***-axis. The 2-fold rotation symmetry relating the Y sites in the cubic structure is lost, creating two distinct Y_1 (red) and Y_2 (cyan) sites.

Figure 6. High-resolution image showing neighboring domains with (101)-glide twin relationship. The fast Fourier transform (FFT) patterns of the two areas show [010] and [001] zone-axis diffraction patterns of the orthorhombic structure respectively, corresponding to the *h*0*l* and *hk*0 sections of the XRD data in Figure 4.

Figure 7. Powder XRD data along with the calculated pattern from the refined orthorhombic structure.

Figure 8. All 6 possible twin orientations of orthorhombic garnet. Only the Y octahedra are shown. Red octahedra are Y_1 (Fe) sites and cyan ones are Y_2 (Al) sites. The twin domains are labeled based on their symmetry relation (twin operation) with the reference domain TD*oo*. The Y sites of TD*oo* are labeled based on the $I\bar{1}$ symmetry in the figure. Note that the same labels apply to all 6 orientations in the figure, because there is no standard or preferred orientation in the triclinic symmetry.

Figure 9. A phase diagram modified from Becker and Pollok (2002) showing stability field for the ordered orthorhombic garnet with $I\frac{2}{a}1\frac{2}{d}$ symmetry at low temperature. Only a temperature of 200 °C for the coexisting andradite and the orthorhombic garnet and data from Jamtveit (1991) with known temperature range of 300 °C – 400 °C are labeled

based on the studied sample. The upper temperature limit for $I\frac{2}{a}1\frac{2}{d}$ structure is not determined.

This is the peer-reviewed, final accepted version for American Mineralogist, published by the Mineralogical Society of America.
The published version is subject to change. Cite as Authors (Year) Title. American Mineralogist, in press.
DOI: https://doi.org/10.2138/am-2022-8455. http://www.minsocam.org/

Appendix

A series of diffraction data of twinned orthorhombic crystals of various proportions are simulated to study the effect of pseudo-merohedral twinning on the structure refinement. The single-crystal data of the orthorhombic structure is simulated using JANA2006 program with a noise level of 1. The data is then multiplied with a twin matrix and added to the original data at a certain ratio. Each resulting simulated data is represented by a 6-digit number which indicates the relative proportion of each individual twin domain (t_{oo}, t_{od}, $t_{od'}$, t_{ao}, t_{ad}, $t_{ad'}$). For example, 111111 is an intergrowth of TDoo, TDo*d*, TDo*d*', TD*a*o, TD*ad*, TD*ad*' twin domains with same volume; 200100 is an intergrowth of TDoo and TD*a*o twin domains with 2:1volume ratio, but without TDo*d*, TDo*d*', TD*ad*, TD*ad*' domains. Although higher (pseudo-)symmetry may be present, we refined all the simulated diffraction data as a single crystal $I\bar{1}$ structure. The resulting Fe occupancies of each Y site are listed in Table A1, along with the R factors of each structure refinement. If higher pseudo-symmetry is present, equivalent Y sites are coded with the same color.

The structure 100100 shows no Fe-Al ordering between Y_1 and Y_2 sites, but the symmetry is still orthorhombic. As discussed in the main text, the (100) glide plane twin law would only switch the positions of Y_1 and Y_2, but keep the Si sites unchanged, which is why even though the Y_1 and Y_2 shows same occupancy, they are still symmetrically different sites. Structure 200100 obviously shows an orthorhombic structure with less ordered Y sites. Structure 111000 shows a [111] 3-fold rotoinversion symmetry. Structure 110110 shows pseudo-tetragonal $I4_1/acd$ space group symmetry with all Y sites equivalent to each other. And with all six twin domains of equal volume to each other, the structure 111111 restores all the symmetry elements in the $Ia\bar{3}d$ space group. It needs to be emphasized that all this pseudosymmetry produced by a certain twin domain component would fail any symmetry test regarding the extinction conditions. All the twinned crystals show no systematic extinctions required for screw axes and glide planes.

The paired-occupancy pattern as discussed in the main text are not exactly followed in the refined structure. This should be expected since the "average" structure of all the twin domains is not really an average of each site in the structure, and there is no symmetry constraint to make the occupancies equal to each other. The intensity of a certain reflection from a single crystal is

This is the peer-reviewed, final accepted version for American Mineralogist, published by the Mineralogical Society of America.
The published version is subject to change. Cite as Authors (Year) Title. American Mineralogist, in press.
DOI: https://doi.org/10.2138/am-2022-8455. http://www.minsocam.org/

proportional to the square of the structure factor, whereas the reflection from a twinned crystal is the arithmetic mean of the intensities from different domains. The difference between Fe occupancies in Y_{1_1} and Y_{1_3} can be up to about 0.1 in structure 210000 and 510000 (refined from simulated twinned diffraction data) (Table A1). It is also interesting that the fake $I\bar{1}$ structure can show an even wider range of Fe occupancies than the real orthorhombic structure, even though the average order between Y_1 and Y_2 is always lower in the $I\bar{1}$ structures. The highest Fe ordering in the limited variations we tested is 0.888 of Y_{1_3} site in the structure 210000 (refined from simulated twinned diffraction data) (Table A1), and the lowest is 0.146 of Y_{2_4} in the same structure.

Table A1: Fe occupancies of the structures refined from simulated diffraction pattern of twinned crystals. The 6-digit number gives the relative proportion of each individual twin domain (TDoo, TDo*d*, TDo*d*', TD*a*o, TD*ad*, TD*ad*'). The difference between the mean occupancies over each quartet of octahedra (x_{Oct1}-x_{Oct2} as defined by Shtukenberg et al, 2005) is also listed in the table for each structure.

Site	Coordinate	Twin Domains and Their Proportions					
		100000	100100	200100	110000	210000	510000
Y_{1_1}	(0,0,0,)	0.8118(8)	0.501(11)	0.666(10)	0.841(7)	0.799(6)	0.800(5)
Y_{1_2}	(1/2,0,0)	0.8121(8)	0.497(11)	0.667(10)	0.551(7)	0.676(6)	0.753(5)
Y_{1_3}	(1/4,1/4,1/4)	0.8137(8)	0.505(11)	0.673(10)	0.843(7)	0.888(6)	0.887(5)
Y_{1_4}	(1/4,1/4,3/4)	0.8140(8)	0.505(11)	0.675(10)	0.484(7)	0.607(6)	0.690(5)
Y_{2_1}	(0,1/2,0)	0.2288(8)	0.497(11)	0.347(10)	0.190(6)	0.236(6)	0.240(5)
Y_{2_2}	(1/2,1/2,0)	0.2284(8)	0.500(11)	0.347(10)	0.482(7)	0.362(6)	0.288(4)
Y_{2_3}	(1/4,3/4,1/4)	0.2297(8)	0.504(11)	0.348(10)	0.549(7)	0.427(6)	0.349(5)
Y_{2_4}	(3/4,1/4,1/4)	0.2287(8)	0.505(11)	0.349(10)	0.188(6)	0.146(6)	0.151(4)
R factor %		0.38	5.48	4.58	2.95	2.63	1.92
Symmetry		Orthorhombic	Orthorhombic	Orthorhombic	Monoclinic	Triclinic	Triclinic
x_{Oct1}-x_{Oct2}		0.584	0.0005	0.3225	0.3275	0.44975	0.5255

Site	Coordinate	Twin Domains and Their Proportions					
		111000	302010	302100	321000	110110	111111
Y_{1_1}	(0,0,0,)	0.823(9)	0.815(8)	0.767(9)	0.811(8)	0.490(13)	0.498(13)
Y_{1_2}	(1/2,0,0)	0.409(9)	0.576(8)	0.488(9)	0.604(8)	0.487(13)	0.489(13)
Y_{1_3}	(1/4,1/4,1/4)	0.857(9)	0.750(8)	0.802(9)	0.879(8)	0.501(13)	0.504(13)
Y_{1_4}	(1/4,1/4,3/4)	0.395(9)	0.663(8)	0.553(9)	0.519(8)	0.515(13)	0.513(13)

This is the peer-reviewed, final accepted version for American Mineralogist, published by the Mineralogical Society of America.
The published version is subject to change. Cite as Authors (Year) Title. American Mineralogist, in press.
DOI: https://doi.org/10.2138/am-2022-8455. http://www.minsocam.org/

Y_{2_1}	(0,1/2,0)	0.407(9)	0.511(8)	0.530(9)	0.283(8)	0.501(13)	0.499(13)
Y_{2_2}	(1/2,1/2,0)	0.408(9)	0.158(8)	0.250(9)	0.367(8)	0.498(13)	0.495(13)
Y_{2_3}	(1/4,3/4,1/4)	0.396(9)	0.211(8)	0.231(9)	0.452(8)	0.514(13)	0.510(13)
Y_{2_4}	(3/4,1/4,1/4)	0.394(9)	0.435(8)	0.477(9)	0.210(8)	0.498(13)	0.495(13)
R factor %		3.87	3.54	4.28	3.54	5.90	6.11
Symmetry		p-Trigonal	Triclinic	Triclinic	Triclinic	p-Tetragonal	p-Cubic
x_{Oct1}-x_{Oct2}		0.21975	0.37225	0.2805	0.37525	-0.0045	0.00125

767

This is the peer-reviewed, final accepted version for American Mineralogist, published by the Mineralogical Society of America.
The published version is subject to change. Cite as Authors (Year) Title. American Mineralogist, in press.
DOI: https://doi.org/10.2138/am-2022-8455. http://www.minsocam.org/

768

Figures

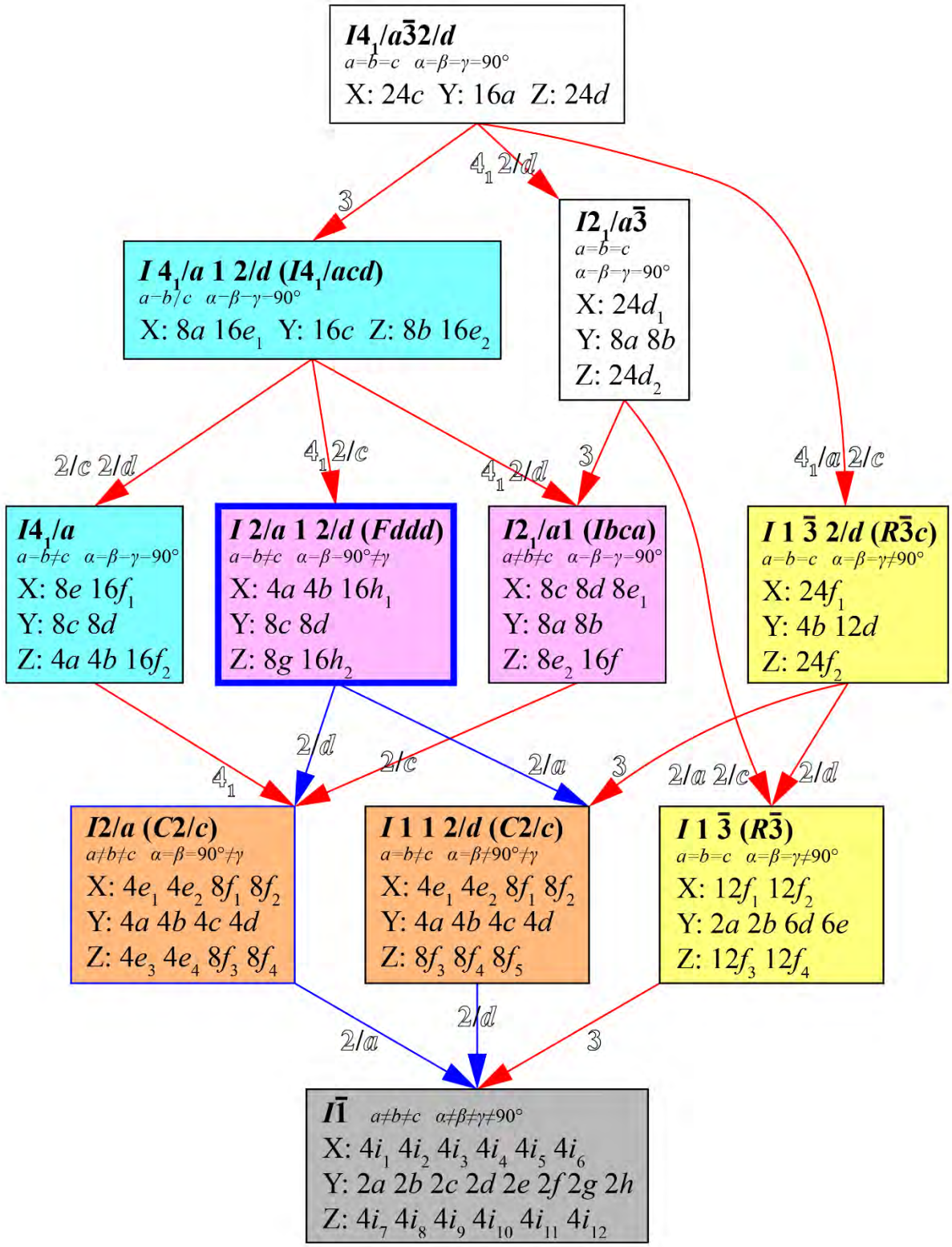

769

770 Figure 1.

771

772

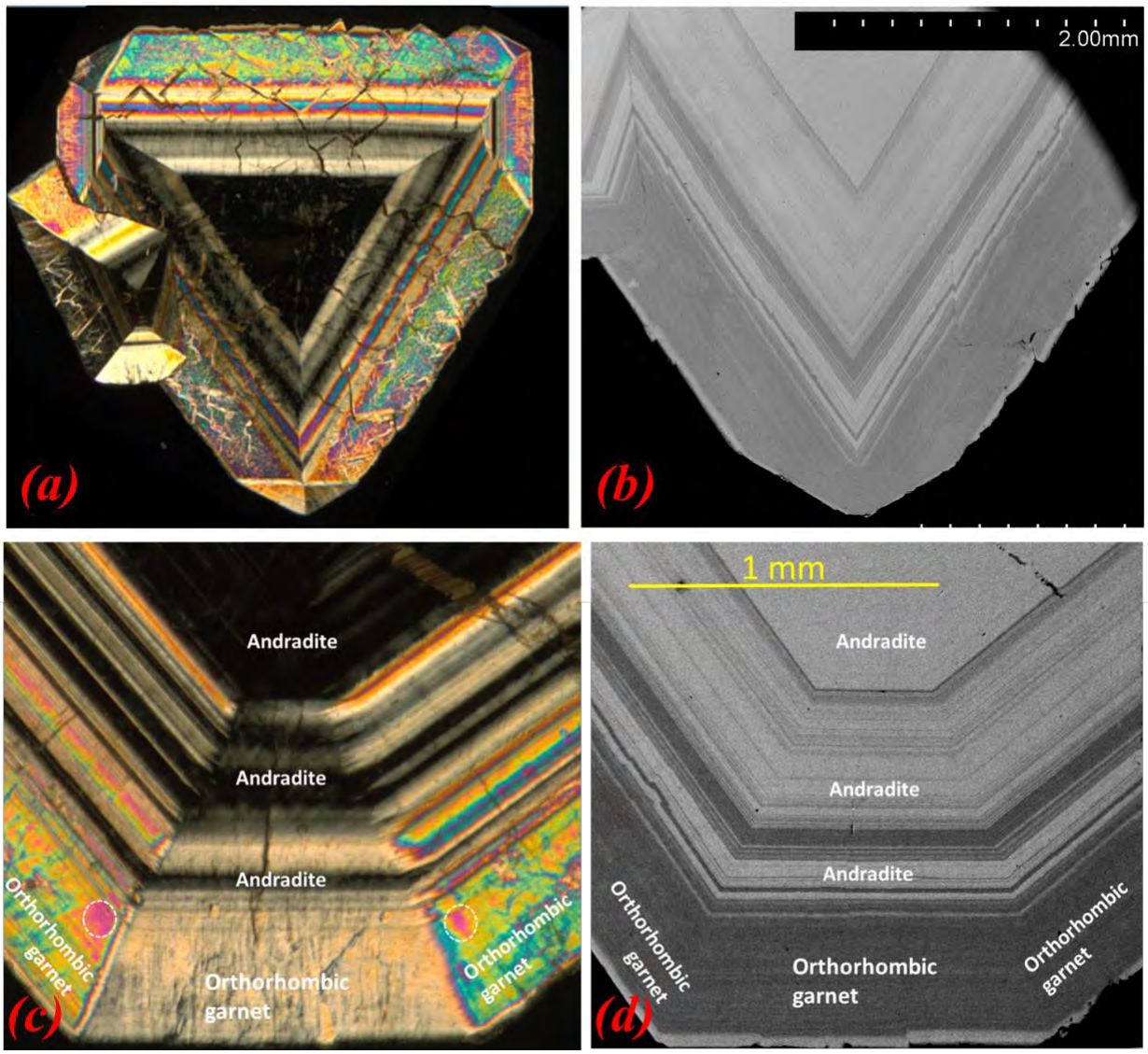

773

774 Figure 2.

775

This is the peer-reviewed, final accepted version for American Mineralogist, published by the Mineralogical Society of America.
The published version is subject to change. Cite as Authors (Year) Title. American Mineralogist, in press.
DOI: https://doi.org/10.2138/am-2022-8455. http://www.minsocam.org/

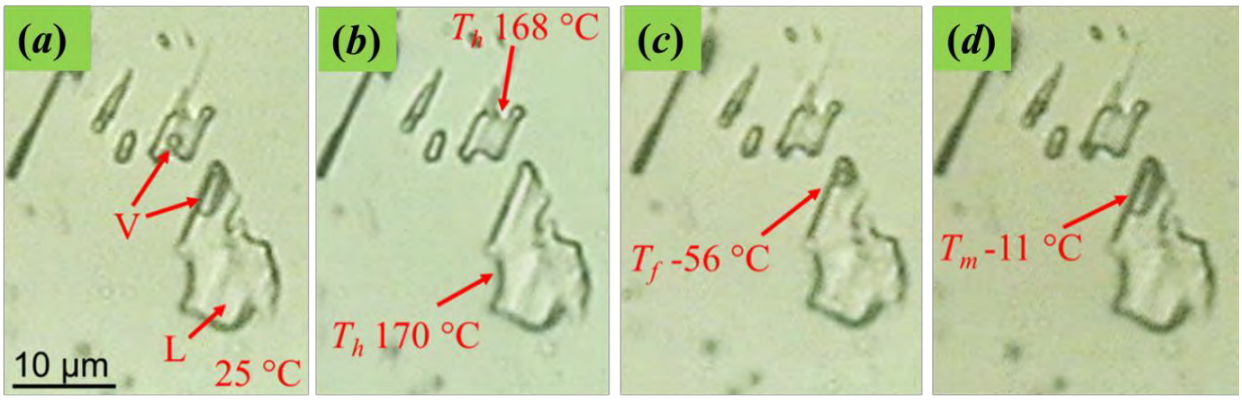

Figure 3.

This is the peer-reviewed, final accepted version for American Mineralogist, published by the Mineralogical Society of America.
The published version is subject to change. Cite as Authors (Year) Title. American Mineralogist, in press.
DOI: https://doi.org/10.2138/am-2022-8455. http://www.minsocam.org/

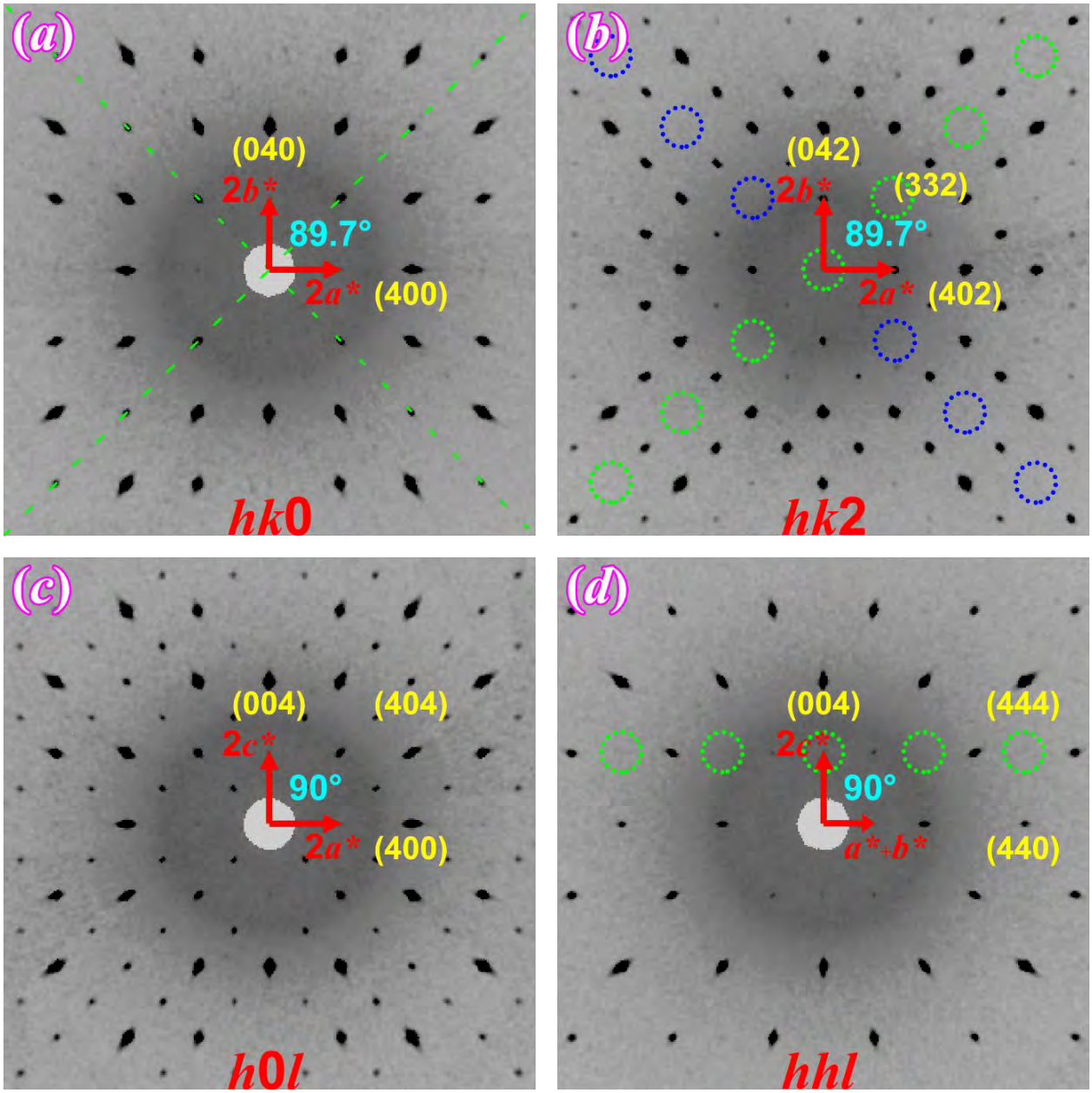

Figure 4.

This is the peer-reviewed, final accepted version for American Mineralogist, published by the Mineralogical Society of America.
The published version is subject to change. Cite as Authors (Year) Title. American Mineralogist, in press.
DOI: https://doi.org/10.2138/am-2022-8455. http://www.minsocam.org/

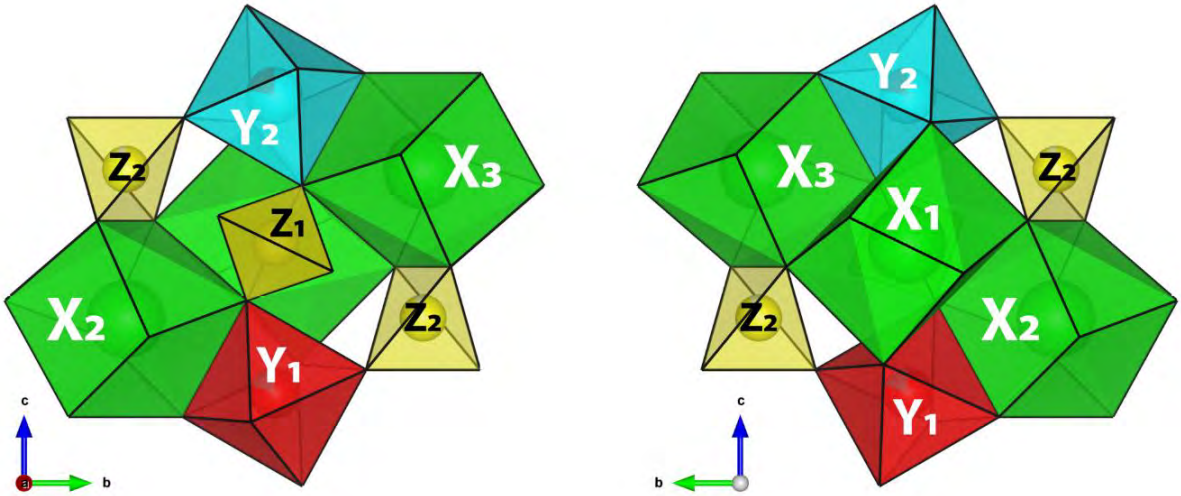

782

783 Figure 5.

784

This is the peer-reviewed, final accepted version for American Mineralogist, published by the Mineralogical Society of America.
The published version is subject to change. Cite as Authors (Year) Title. American Mineralogist, in press.
DOI: https://doi.org/10.2138/am-2022-8455. http://www.minsocam.org/

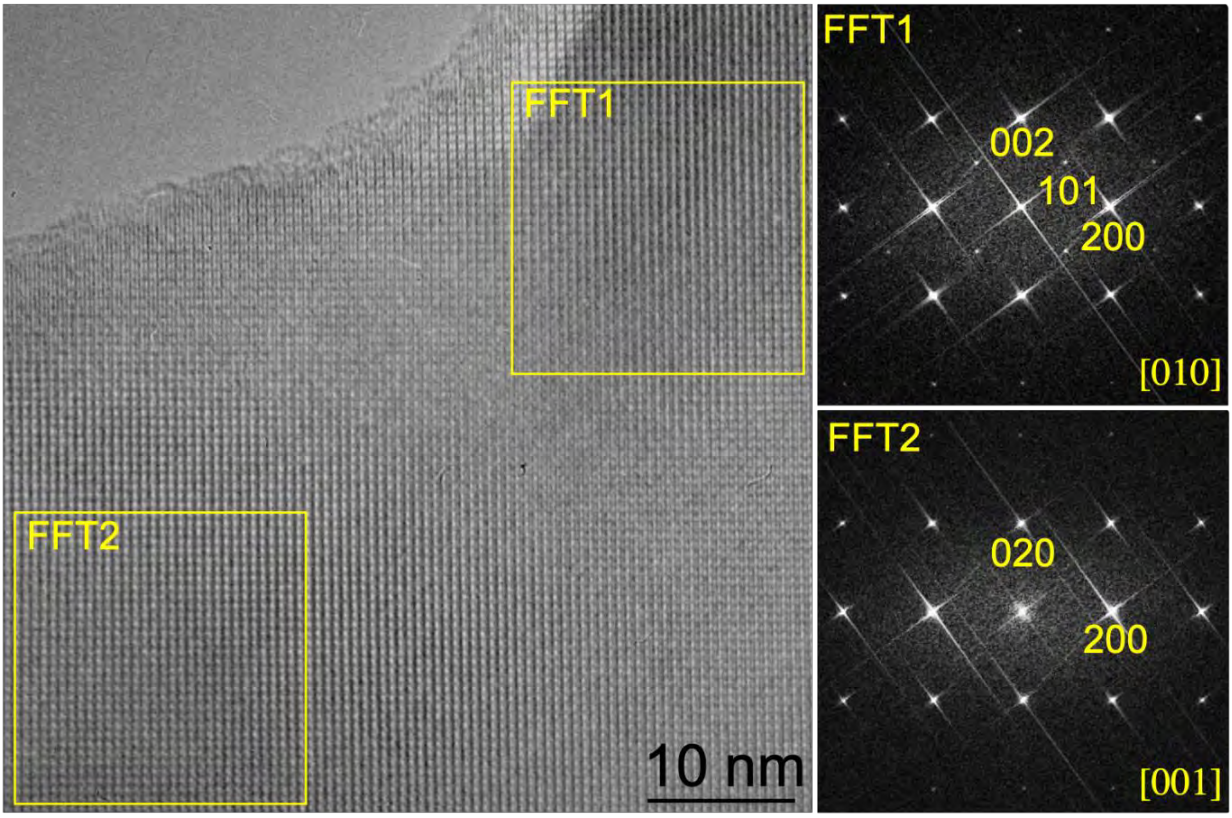

Figure 6.

This is the peer-reviewed, final accepted version for American Mineralogist, published by the Mineralogical Society of America.
The published version is subject to change. Cite as Authors (Year) Title. American Mineralogist, in press.
DOI: https://doi.org/10.2138/am-2022-8455. http://www.minsocam.org/

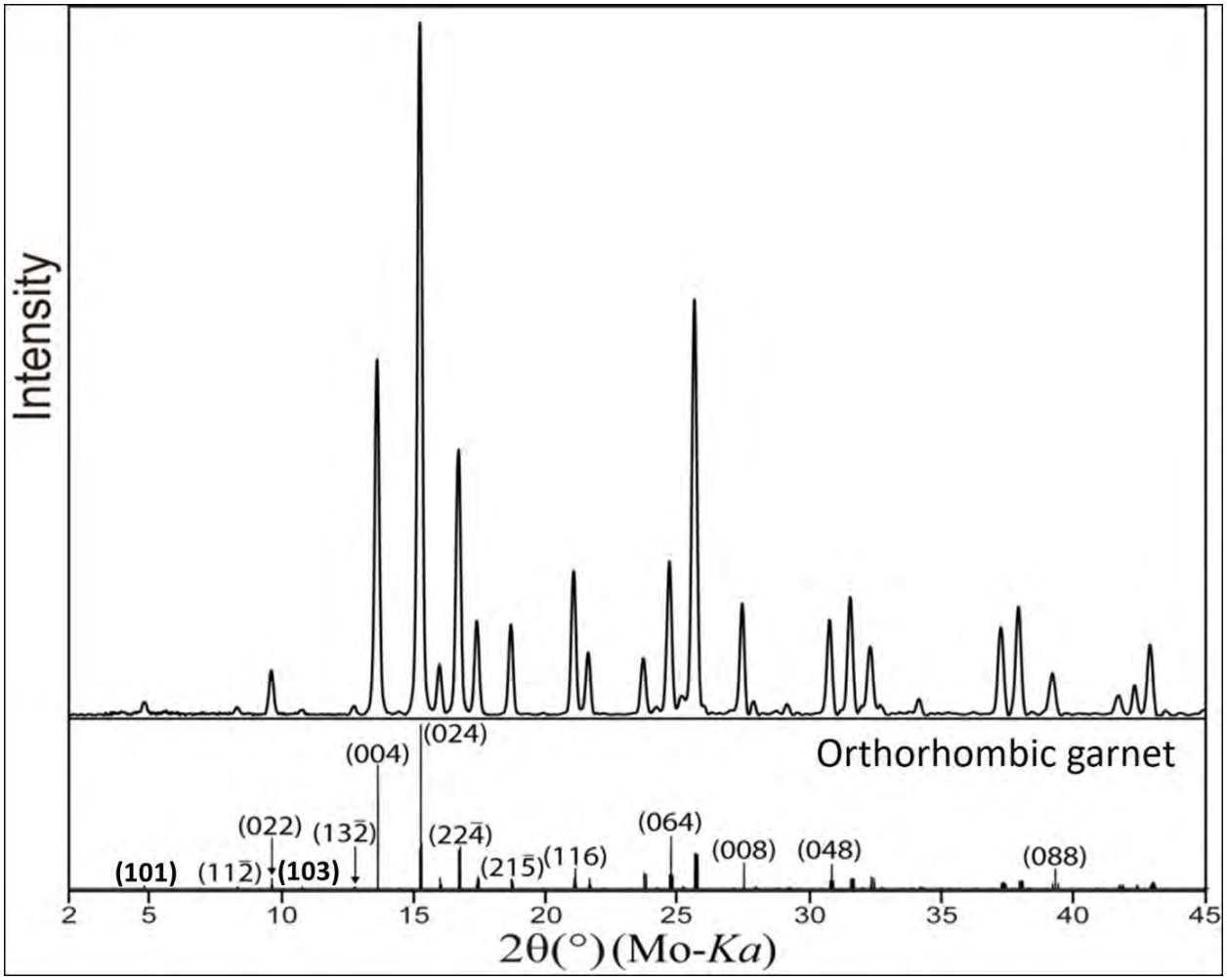

788

789 Figure 7.

790

This is the peer-reviewed, final accepted version for American Mineralogist, published by the Mineralogical Society of America.
The published version is subject to change. Cite as Authors (Year) Title. American Mineralogist, in press.
DOI: https://doi.org/10.2138/am-2022-8455. http://www.minsocam.org/

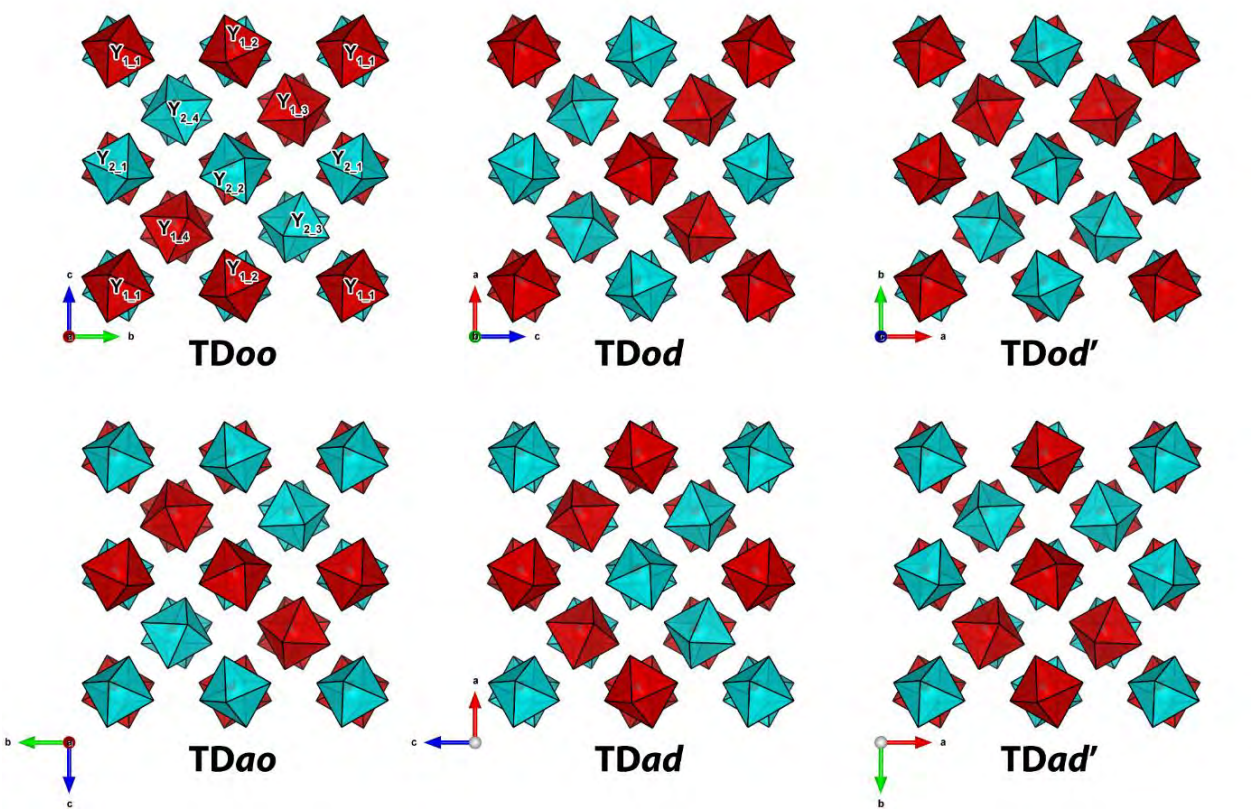

Figure 8.

794

795

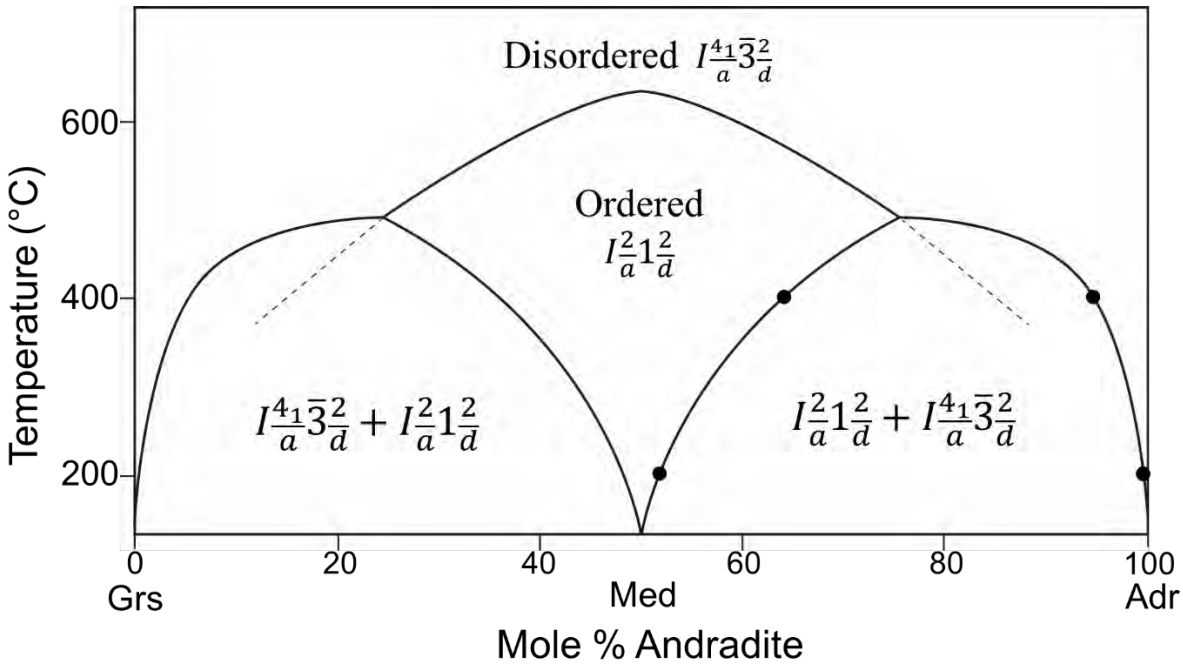

796

797 Figure 9.

798

This is the peer-reviewed, final accepted version for American Mineralogist, published by the Mineralogical Society of America.
The published version is subject to change. Cite as Authors (Year) Title. American Mineralogist, in press.
DOI: https://doi.org/10.2138/am-2022-8455. http://www.minsocam.org/

Tables

Table 1. Chemical data for orthorhombic garnet and andradite collected from areas in Figure. 2

Element	Orthorhombic Garnet							Andradite				Intermediate	
Wt%	1	2	3	4	5	6	Avg	1	2	3	Avg	1	2
Si	17.05	16.94	17.33	17.20	17.24	16.99	17.12	16.38	16.29	16.45	16.37	16.70	16.35
Al	5.33	5.37	5.34	5.27	5.16	5.32	5.30	0.01	0.00	0.02	0.01	2.62	2.35
Ca	24.43	24.20	24.31	24.33	24.30	24.35	24.32	23.15	23.19	23.09	23.14	24.00	24.12
Fe	13.08	13.05	12.88	12.84	13.26	12.98	13.01	22.09	22.15	22.33	22.19	17.64	17.89
Mn	0.23	0.26	0.33	0.28	0.29	0.29	0.28	0.13	0.15	0.11	0.13	0.20	0.29
O	39.39	39.54	39.56	39.61	39.41	39.55	39.51	37.48	37.66	37.54	37.56	38.65	38.71
F	0.46	0.57	0.71	0.53	0.43	0.67	0.56	0.24	0.24	0.38	0.29	0.30	0.38
Total	99.96	99.93	100.46	100.07	100.08	100.13	100.11	99.47	99.68	99.92	99.69	100.11	100.08
	Site occupancy												
Ca^{2+}	2.94	2.90	2.90	2.91	2.93	2.91	2.91	2.94	2.94	2.92	2.93	2.96	2.96
Fe^{2+}	0.08	0.08	0.05	0.04	0.07	0.06	0.06	0.02	0.01	0.03	0.02	0.04	0.00
Mn^{2+}	0.02	0.02	0.03	0.02	0.03	0.03	0.02	0.01	0.01	0.01	0.01	0.02	0.03
$^{X}\Sigma$	3.05	3.00	2.98	2.97	3.02	2.99	3.00	2.97	2.96	2.96	2.97	3.01	2.99
Fe^{3+}	1.05	1.05	1.05	1.06	1.08	1.06	1.06	2.00	2.00	2.00	2.00	1.52	1.57
Al^{3+}	0.95	0.95	0.95	0.94	0.92	0.94	0.94	0.00	0.00	0.01	0.00	0.48	0.43
$^{Y}\Sigma$	2.00	2.00	2.00	2.00	2.00	2.00	2.00	2.00	2.00	2.00	2.00	2.00	2.00
Si^{4+}	2.93	2.89	2.95	2.93	2.96	2.90	2.93	2.97	2.94	2.97	2.96	2.94	2.86
□	0.07	0.11	0.05	0.07	0.04	0.11	0.07	0.03	0.06	0.03	0.04	0.07	0.14
$^{Z}\Sigma$	3.00	3.00	3.00	3.00	3.00	3.00	3.00	3.00	3.00	3.00	3.00	3.00	3.00
O^{2-}	11.81	11.57	11.75	11.68	11.89	11.55	11.71	11.83	11.69	11.81	11.78	11.76	11.44
F^{-}	0.12	0.14	0.18	0.14	0.11	0.17	0.14	0.07	0.06	0.10	0.08	0.08	0.10
OH^{-}	0.07	0.29	0.07	0.18	0.00	0.28	0.15	0.11	0.25	0.09	0.15	0.16	0.47
$^{\phi}\Sigma$	12.00	12.00	12.00	12.00	12.00	12.00	12.00	12.00	12.00	12.00	12.00	12.00	12.00

*All the cations are normalized to 12 (O+F) and number for H (or OH) is calculated based on charge balance.

This is the peer-reviewed, final accepted version for American Mineralogist, published by the Mineralogical Society of America.
The published version is subject to change. Cite as Authors (Year) Title. American Mineralogist, in press.
DOI: https://doi.org/10.2138/am-2022-8455. http://www.minsocam.org/

Table 2. Experimental details of X-ray diffraction and structure refinement.

Crystal data	
Chemical formula	$Ca_3(Fe_{0.804}Al_{0.196})(Al_{0.779}Fe_{0.221})(Si_{2.917}\square_{0.083})O_{12}$
Color	yellow-brownish green
Crystal size (mm)	0.09×0.09×0.06
Temperature (K)	298
Crystal System	Orthorhombic
Space Group	$I\frac{2}{a}1\frac{2}{d}$ $(Fddd)$
a, b, c (Å)	11.966(3)
	11.966(3)
	11.964(3)
α, β, γ (°)	90
	90
	90.29(2)
V (Å^3)	1713.0(7)
Data collection	
Exposure time (s/frame)	40
Scanning width (°)	0.5
Runs	3ω+1φ
Total reflections	15579
Independent reflections	1318
observed [I > 3σ(I)] reflections	963
R_{int}	0.081
θ values (°)	θ_{max} = 30.5,
	θ_{min} = 2.4
(sin θ/λ) max (Å^{-1})	0.715
Range of *h, k, l*	*h* = -17→16
	k = -17→17
	l = -17→15
Refinement	
R[F^2>3σ (F^2)]	0.0194
wR^2[F^2>3σ (F^2)]	0.0638
R(all)	0.0268
wR^2(all)	0.0668
GOF(obs)	1.05
GOF(all)	1.19
No. of parameters	100
No. of constraints	12
$\Delta\rho_{max}$, $\Delta\rho_{min}$ (eÅ^{-3})	0.31, -0.27

This is the peer-reviewed, final accepted version for American Mineralogist, published by the Mineralogical Society of America.
The published version is subject to change. Cite as Authors (Year) Title. American Mineralogist, in press.
DOI: https://doi.org/10.2138/am-2022-8455. http://www.minsocam.org/

Table 3. Intensity statistics of the integrated peaks for different space groups using the absorption-corrected data (multi-scan method in Laue group $\bar{1}$).

Space Group	Point Group	R_{int}(obs/all)	# averaged	Redundancy	Systematic Extinction (obs/all)
$I\bar{1}$	$\bar{1}$	1.68/1.75	3421/5208	3.225	0/0
$I\frac{2}{a}$	$\frac{2}{m}$	1.82/1.89	1907/2735	6.141	3/451
$I11\frac{2}{d}$ (***a+b***)	$\frac{2}{m}$	1.87/1.93	1894/2703	6.213	10/304
$I11\frac{2}{d}$ (***a-b***)	$\frac{2}{m}$	1.90/1.97	1903/2704	6.211	2/243
$I\frac{2}{a}1\frac{2}{d}$	$\frac{2}{m}\frac{2}{m}\frac{2}{m}$	1.96/2.02	1069/1455	11.543	12/928
$I\frac{4_1}{a}1\frac{2}{d}$	$\frac{4}{m}\frac{2}{m}\frac{2}{m}$	6.71/6.74	653/792	21.206	435/1707
$I\frac{4_1}{a}\bar{3}\frac{2}{d}$	$\frac{4}{m}\bar{3}\frac{2}{m}$	7.38/7.40	277/297	56.549	745/2659

This is the peer-reviewed, final accepted version for American Mineralogist, published by the Mineralogical Society of America.
The published version is subject to change. Cite as Authors (Year) Title. American Mineralogist, in press.
DOI: https://doi.org/10.2138/am-2022-8455. http://www.minsocam.org/

Table 4. Atom coordination and occupancies of the refined structure in the body-centered pseudo-cubic cell setting.

Site	Atom	Occ.	x	y	z	U_{equiv}	Multiplicity
X_1	Ca	1	0.24962(3)	0.37526(3)	0.50068(2)	0.00760(10)	16
X_2	Ca	1	0	0.25	0.125	0.00787(13)	4
X_3	Ca	1	0	0.25	0.625	0.00772(13)	4
Y_1	Fe	0.804(3)	0	0	0	0.00590(12)	8
	Al	0.196(3)					
Y_2	Al	0.779(3)	0	0	0.5	0.00458(17)	8
	Fe	0.221(3)					
Si_1	Si	0.987(2)	0.24871(3)	0.12523(3)	0.50188(3)	0.00558(14)	16
Si_2	Si	0.936(2)	0	0.25	0.37632(4)	0.00469(18)	8
O_1	O	1	0.65182(8)	0.03911(8)	0.04540(8)	0.0095(3)	16
O_2	O	1	0.04825(8)	0.65426(8)	0.03938(8)	0.0101(3)	16
O_3	O	1	0.03821(8)	0.04671(7)	0.65148(8)	0.0091(3)	16
O_4	O	1	0.34486(7)	0.53948(8)	0.45162(8)	0.0092(3)	16
O_5	O	1	0.04656(8)	0.34807(8)	0.46275(8)	0.0098(3)	16
O_6	O	1	0.46078(8)	0.04677(8)	0.34455(8)	0.0093(3)	16

This is the peer-reviewed, final accepted version for American Mineralogist, published by the Mineralogical Society of America.
The published version is subject to change. Cite as Authors (Year) Title. American Mineralogist, in press.
DOI: https://doi.org/10.2138/am-2022-8455. http://www.minsocam.org/

Table 5. Anisotropic temperature parameters of atoms in the refined structure.

		U^{11}	U^{22}	U^{33}	U^{12}	U^{13}	U^{23}
X_1	Ca	0.00786(17)	0.00584(17)	0.00911(19)	0.00117(14)	0.00097(9)	-0.00002(9)
X_2	Ca	0.00832(18)	0.00832(18)	0.0070(3)	0.0020(2)	0	0
X_3	Ca	0.00825(18)	0.00825(18)	0.0066(3)	0.0002(2)	0	0
Y_1	Fe	0.0056(2)	0.0055(2)	0.0066(2)	0.00108(13)	0.00002(10)	-0.00009(10)
Y_2	Al	0.0042(3)	0.0045(3)	0.0050(3)	0.0012(2)	-0.00002(15)	-0.00048(15)
Si_1	Si	0.0052(2)	0.0050(2)	0.0066(3)	0.00114(19)	0.00012(13)	0.00015(13)
Si_2	Si	0.0048(3)	0.0049(3)	0.0044(4)	0.0009(2)	0	0
O_1	O	0.0091(5)	0.0094(5)	0.0101(5)	0.0017(4)	0.0004(4)	-0.0008(4)
O_2	O	0.0095(5)	0.0088(5)	0.0119(5)	0.0010(4)	-0.0005(4)	0.0011(4)
O_3	O	0.0081(4)	0.0095(5)	0.0096(5)	0.0007(4)	-0.0005(4)	0.0004(4)
O_4	O	0.0090(5)	0.0087(5)	0.0099(5)	0.0012(4)	0.0000(4)	-0.0009(4)
O_5	O	0.0086(5)	0.0096(5)	0.0113(5)	0.0017(4)	0.0006(4)	0.0009(4)
O_6	O	0.0092(5)	0.0089(4)	0.0099(5)	0.0004(3)	0.0000(4)	-0.0003(4)

This is the peer-reviewed, final accepted version for American Mineralogist, published by the Mineralogical Society of America.
The published version is subject to change. Cite as Authors (Year) Title. American Mineralogist, in press.
DOI: https://doi.org/10.2138/am-2022-8455. http://www.minsocam.org/

Table 6. All the bond distances (Å) in the structure.

Site	oxygen site	bond distance	Site	oxygen site	bond distance
X_1 (Ca) (16)	O_1	2.3500(14)	Y_1 (Fe) (8)	O_2	1.9878(13)
	O_1	2.5050(15)		O_6	2.0011(13)
	O_2	2.4894(15)		O_4	2.0033(13)
	O_3	2.3437(13)		average	1.9974(13)
	O_4	2.3413(14)	Y_2 (Al) (8)	O_1	1.9508(13)
	O_4	2.4914(15)		O_3	1.9503(13)
	O_5	2.4915(13)		O_5	1.9556(13)
	O_6	2.3444(13)		average	1.9522(13)
	average	2.4196(14)	Si_1 (16)	O_1	1.6474(12)
X_2 (Ca) (4)	O_2	2.3496(13)		O_3	1.6463(11)
	O_6	2.5013(15)		O_4	1.6425(12)
	average	2.4255(14)		O_6	1.6428(11)
X_3 (Ca) (4)	O_3	2.4975(15)		average	1.6448(11)
	O_5	2.3344(13)	Si_2 (8)	O_2	1.6537(11)
	average	2.4160(14)		O_5	1.6584(11)
Ca average	Ca average	2.4203(14)		average	1.6561(11)